Trends of higher-order exchange interactions in transition metal trilayers

Mara Gutzeit, Soumyajyoti Haldar,* Sebastian Meyer,† and Stefan Heinze
Institute of Theoretical Physics and Astrophysics, University of Kiel, Leibnizstrasse 15, 24098 Kiel, Germany

(Received 20 April 2021; revised 29 June 2021; accepted 29 June 2021; published 14 July 2021)

We present a systematic study of higher-order exchange interactions beyond the pairwise Heisenberg exchange in transition metal trilayers based on density functional theory calculations. We show that these terms can play an important role in magnetic trilayers composed of a single hexagonal Fe or Co atomic layer sandwiched between 4*d* and 5*d* transition metal layers. We study the dependence of the biquadratic and the three-site and four-site four spin interaction on the band filling of the 4*d* and 5*d* layers as well as the stacking sequence, i.e., fcc vs. hcp stacking. Our calculations reveal relatively small higher-order interactions for Co based trilayers. For Fe based trilayers with a Rh or Ir layer the higher-order terms can be on the same order of magnitude as pairwise Heisenberg exchange. The trends obtained for freestanding trilayers are used to understand the higher-order interactions in ultrathin film systems on surfaces that are experimentally accessible. It is shown that hcp-Rh/Fe/Ir(111) and hcp-Rh/Fe/Rh(111) exhibit the largest values for the biquadratic and the three-site four spin interaction of all systems under study. We further demonstrate that the three-site four spin interaction is responsible for the experimentally observed change of the magnetic ground state of Rh/Fe/Ir(111) from a spin spiral (single-Q) for fcc-Rh to a $2Q$ state for hcp-Rh. We find similar trends for Rh/Fe/Rh(111), i.e., replacing the Ir surface by the isoelectronic Rh surface. For Rh/Co/Ir(111), we obtain a negative value for the four-site four spin interaction which will lead to a reduced stability of magnetic skyrmions which are metastable in this film at zero magnetic field. In contrast, for Pd/Fe/Ir(111), the four-site four spin interaction is positive which leads to an enhanced stability of skyrmions.

DOI: 10.1103/PhysRevB.104.024420

I. INTRODUCTION

The magnetic properties of a material are commonly discussed starting from the Heisenberg model which rests on the exchange interaction between pairs of magnetic moments. For metals, the pairwise exchange interaction can be obtained in second order perturbation theory from the Hubbard model which describes electrons on a lattice by their hopping between sites and their mutual Coulomb repulsion. However, spin interactions beyond the conventional Heisenberg exchange arise if one includes higher-order terms in the perturbative expansion. It has been shown that the two-site four spin (biquadratic) and the four-site four spin interaction occur in fourth order for the spin-1/2 Hubbard model [1,2]. Recently, it has been demonstrated that in addition a three-site four spin interaction arises if one considers systems with a spin $S \geqslant 1$ [3] appropriate in spin models for 3*d* transition metals such as Co, Fe, or Mn with magnetic moments on the order of 2 to 3 μ_B.

Higher-order exchange interactions (HOI) beyond the conventional pairwise Heisenberg exchange can play a crucial role for the magnetic properties of transition metal nanostructures. A model class of material systems consists of monolayers of magnetic 3*d* transition metals on 4*d* and 5*d* transition metal surfaces allowing a pseudomorphic growth of the 3*d* monolayer and experimental accessibility [4,5]. Prominent examples of complex noncollinear magnetic ground states driven by HOI are the triple-Q state first proposed by Kurz *et al.* [6] and recently experimentally observed in a Mn monolayer on the Re(0001) surface [7] as well as the conical spin spiral ground state of a Mn double layer on W(110) [8]. The interplay with the Dzyaloshinskii-Moriya interaction (DMI), which occurs due to spin-orbit coupling in systems with broken inversion symmetry, even leads to the formation of a nanoskyrmion lattice in an Fe monolayer on Ir(111) [9]. The coupling of spin spirals via HOI can also result in collinear magnetic ground states such as the up-up-down-down (*uudd*) or double-row wise antiferromagnetic state [10,11]. Recently, it has been shown that the *uudd* state can be triggered by the three-site four spin interaction [3] and it was experimentally observed in an Fe monolayer on the Rh(111) surface [12].

The magnetic properties in such systems can be tuned by adding another interface, e.g., by growing a nonmagnetic overlayer on the 3*d* transition metal films as in the Rh/Fe atomic bilayer on Ir(111) [13]. In the latter system, there is a surprising dependence of the magnetic ground state on the stacking of the Rh overlayer. While a spin spiral state has been found for fcc-Rh stacking, a canted *uudd* state exists for hcp-Rh stacking [13]. The canting is induced by the competition of the HOI and the DMI, however, the origin of the stacking dependence in terms of the involved HOI has not yet been explained. Recently, a stacking-dependent change of the sign

*haldar@physik.uni-kiel.de
†Present address: Nanomat/Q-mat/CESAM, Universitè de Liège, B-4000 Sart Tilman, Belgium.

of the four-site four spin interaction has been reported for a Pd/Fe atomic bilayer on the Re(0001) surface [14]. The four-site four spin interaction plays an important role for the stability of topological spin structures such as skyrmions and antiskyrmions which has been exemplified for Pd/Fe bilayers on Rh(111) and Ir(111) [15].

So far a systematic study about HOI at transition metal interfaces is missing and only the Fe and Mn based ultrathin film systems mentioned above have been a matter of both theoretical and experimental research. Although isolated nanometer skyrmions were observed in Rh/Co bilayers on Ir(111) as well [16], no studies for HOI terms which could potentially contribute to the stabilization of these particlelike spin structures in Co based systems are available yet. However, a more systematic investigation would shed light on the question whether these systems can be regarded as special or if there exits a trend indicating which types of transition metal surfaces might show large effects on the HOI terms.

Here, we investigate based on density functional theory (DFT) as implemented in the FLEUR [17] code and in the VASP code [18] how pairwise Heisenberg and higher-order exchange constants are modified at transition metal interfaces. We consider freestanding trilayers and start with Rh/Fe/Ir which serves as a simplified model of the film system Rh/Fe/Ir(111). In our first-principles calculations, we replace either the Rh layer by another 4*d* transition metal or the Ir layer by another 5*d* transition metal. Thereby, we can increase or decrease the 4*d* or 5*d* band filling which influences the hybridization with the 3*d* Fe states and via changes in the electronic structure also the magnetic interactions. Since a strong influence of the stacking sequence has been reported for Rh/Fe/Ir(111), we compare fcc and hcp stacking in our theoretical study. Finally, we replace the Fe layer by a Co layer to investigate the effect of changing the transition metal with the intrinsic magnetic moment and to obtain results for the effect of higher-order interactions in Co. From the freestanding trilayers we find a number of interesting trends concerning the pairwise and higher-order exchange interactions at such transition metal interfaces. We compare these trends with the results obtained for selected ultrathin film systems which are amenable to experiments.

The structure of the paper is as follows. First, we introduce the atomistic spin model including all relevant magnetic interactions which we calculated using DFT as well as the applied computational methods in Secs. II A and II B, respectively. The main part of the paper (Sec. III) covers both results and discussions for the investigated Fe and Co based trilayer systems separately as well as a comparison between the properties of the two of them. We relate the freestanding trilayer calculations to those for ultrathin films on surfaces which have in the past partly been studied by scanning tunneling microscopy (STM) experiments. Finally, we summarize our main conclusions in Sec. IV.

II. COMPUTATIONAL DETAILS

A. Atomistic spin model

In order to describe the magnetic properties of transition metal trilayers we resort to an extended version of the classical Heisenberg model dealing with magnetic moments $\mathbf{M}_i$ localized at atomic sites i of a hexagonal lattice:

$$\begin{aligned}\mathcal{H} = &-\sum_{ij} J_{ij}(\mathbf{m}_i \cdot \mathbf{m}_j) - \sum_{ij} B_{ij}(\mathbf{m}_i \cdot \mathbf{m}_j)^2 \\ &- \sum_{ijkl} K_{ijkl}[(\mathbf{m}_i \cdot \mathbf{m}_j)(\mathbf{m}_k \cdot \mathbf{m}_l) + (\mathbf{m}_i \cdot \mathbf{m}_l)(\mathbf{m}_j \cdot \mathbf{m}_k) \\ &- (\mathbf{m}_i \cdot \mathbf{m}_k)(\mathbf{m}_j \cdot \mathbf{m}_l)] \\ &- \sum_{ijk} Y_{ijk}[(\mathbf{m}_i \cdot \mathbf{m}_j)(\mathbf{m}_j \cdot \mathbf{m}_k) + (\mathbf{m}_j \cdot \mathbf{m}_i)(\mathbf{m}_i \cdot \mathbf{m}_k) \\ &+ (\mathbf{m}_i \cdot \mathbf{m}_k)(\mathbf{m}_k \cdot \mathbf{m}_j)]. \end{aligned} \tag{1}$$

Here we use the normalized vector of the magnetic moment, $\mathbf{m}_i = \mathbf{M}_i/M_i$. The first contribution to the Hamiltonian comes from the pairwise Heisenberg exchange interaction which can be derived in second order perturbation theory from the Hubbard model for spin-1/2 particles in case the Coulomb interaction is large compared to the hopping of electrons [2,19]. The sign of the exchange constant J_{ij} determines whether a parallel orientation, i.e., a ferromagnetic (FM) coupling ($J > 0$), or an antiparallel ordering, i.e., an antiferromagnetic (AFM) coupling ($J < 0$) between moments $\mathbf{m}_i$ and $\mathbf{m}_j$ is favored by this bilinear interaction. Different signs of the corresponding exchange constants J_{ij} result in frustration which can lead to a tilting of the magnetic moments thereby being the origin of noncollinear spin structures such as spin spirals.

The second part of the Hamiltonian of Eq. (1) describes the biquadratic exchange, an interplay which involves four times the hopping of an electron between the two lattice sites i and j thereby representing a so-called two-site four spin interaction. As for the Heisenberg exchange, the biquadratic constant B_{ij} is identical for symmetry equivalent pairs of spins. In this paper only biquadratic exchange with nearest neighbors is taken into account as shown in Fig. 1.

Expanding the Hubbard model up to fourth order perturbation theory in the limit of large Coulomb energy U with respect to the hopping parameter t [1], one finds in addition the four-site four spin interaction characterized by the parameter K_{ijkl} [cf. Eq. (1)]. Allowing an electron to hop over four lattice sites i, j, k, l, one finds closed hopping paths taking the shape of a diamond on the hexagonal lattice within the nearest-neighbor (NN) approximation (see Fig. 1).

The last interaction considered here and listed as the fourth contribution in Eq. (1) has recently been derived from a multiband Hubbard model [3] in fourth order perturbation theory: the three-site four spin interaction. In contrast to the previously mentioned contribution to the Hamiltonian, this term leads to triangle shaped hopping paths for an electron on the hexagonal lattice which is highlighted in orange color in Fig. 1.

In the following we denote the biquadratic, four-site four spin and three-site four spin interaction by B_1, K_1, and Y_1, respectively, in order to bear the NN approximation in mind. Since the exchange interactions are our focus in this work we neglect—both in the Hamiltonian [Eq. (1)] and in our DFT calculations—the influence of spin-orbit coupling which is the origin of the Dzyaloshinskii-Moriya interaction, the

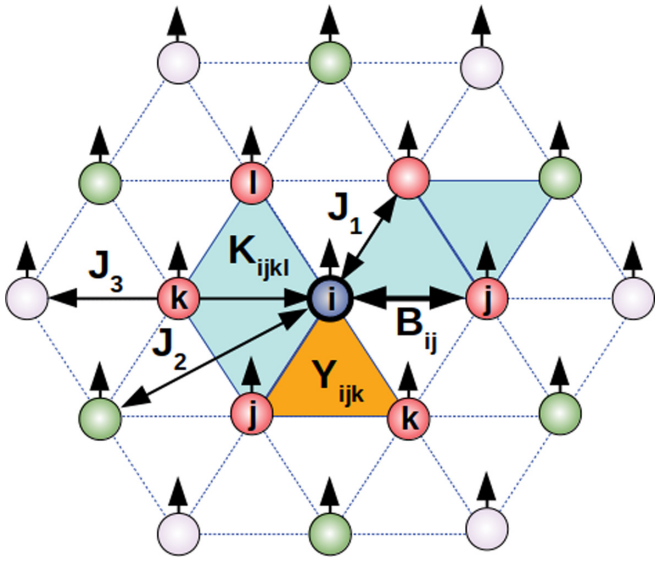

FIG. 1. Schematic representation of the four considered magnetic exchange interactions on the two-dimensional hexagonal lattice. The reference atom is depicted in blue color, its nearest neighbors are marked in red, the next-nearest in green and the third nearest in light blue color. Whereas both the pairwise Heisenberg (shown up to the third-nearest neighbor) and the biquadratic exchange involve only two lattice sites, the three-site four spin interaction contains electron hopping over the three lattice sites *ijk* thereby forming a triangle depicted in orange. One out of the 6 possible triangles is illustrated. The four-site four spin interaction on the other hand includes hopping of electrons over the four sites *ijkl* resulting in a diamond shape. Two out of 12 possible diamonds for the nearest-neighbor (NN) approximation are depicted in blue color.

magnetocrystalline anisotropy, and recently proposed multi-spin chiral interactions [20–23].

Now we turn our focus to the question of how these exchange constants can be calculated by means of DFT. To obtain the pairwise exchange constants, we use the energy dispersion of spin spirals. Spin spirals are characterized by a spin spiral vector $\mathbf{q}$ and describe spin structures with magnetic moments tilted by a constant angle for adjacent moments along the direction given by $\mathbf{q}$. Hence the moment at lattice site $\mathbf{R}_i$ is given by $\mathbf{M}_i = M(\cos(\mathbf{q}\cdot\mathbf{R}_i), \sin(\mathbf{q}\cdot\mathbf{R}_i), 0)$, where M is the constant magnitude of the magnetic moment at all sites. Since spin spirals represent the general solution of the classical Heisenberg model on a periodic lattice, the pairwise exchange constants can be obtained from fitting energy dispersions $E(\mathbf{q})$ of flat homogeneous spin spirals along the high symmetry directions $\overline{\Gamma\mathrm{M}}$ and $\overline{\Gamma\mathrm{KM}}$ of the two-dimensional (2D) hexagonal Brillouin zone (BZ) [see Fig. 2(b)]. At the center of the 2D BZ, i.e., at $\mathbf{q} = 0$ represented by the $\overline{\Gamma}$ point the FM state occurs, whereas at the $\overline{\mathrm{M}}$ point the row-wise antiferromagnetic (RW-AFM) state and at the $\overline{\mathrm{K}}$ point the Néel state with angles of 120° between adjacent moments can be found. Note that we restrict the discussion of trends to Heisenberg exchange constants up to the third nearest neighbor (Fig. 1). However, the fitting of the energy dispersion of spin spirals has been performed with exchange up to eight nearest neighbors.

A superposition of spin spirals—also referred to as $1Q$ states—with symmetry equivalent $\mathbf{q}$ vectors can lead to the formation of multi-Q states. A prominent example is the collinear *uudd* or double-row wise antiferromagnetic state [10] originating from a superposition of two counterpropagating 90° spin spirals [see Fig. 2(a)]. In the 2D hexagonal BZ there are two possibilities to obtain a 90° spin spiral and hence an *uudd* state by the superposition of its left- and right-rotating counterpart at $\mathbf{q} = \pm\frac{1}{2}\overline{\Gamma\mathrm{M}}$ and $\mathbf{q} = \pm\frac{3}{4}\overline{\Gamma\mathrm{K}}$ [Fig. 2(b)]. A third multi-Q state needed for the evaluation of the HOI parameters is the $3Q$ state [6], a three-dimensional noncollinear spin structure on the 2D lattice formed by a

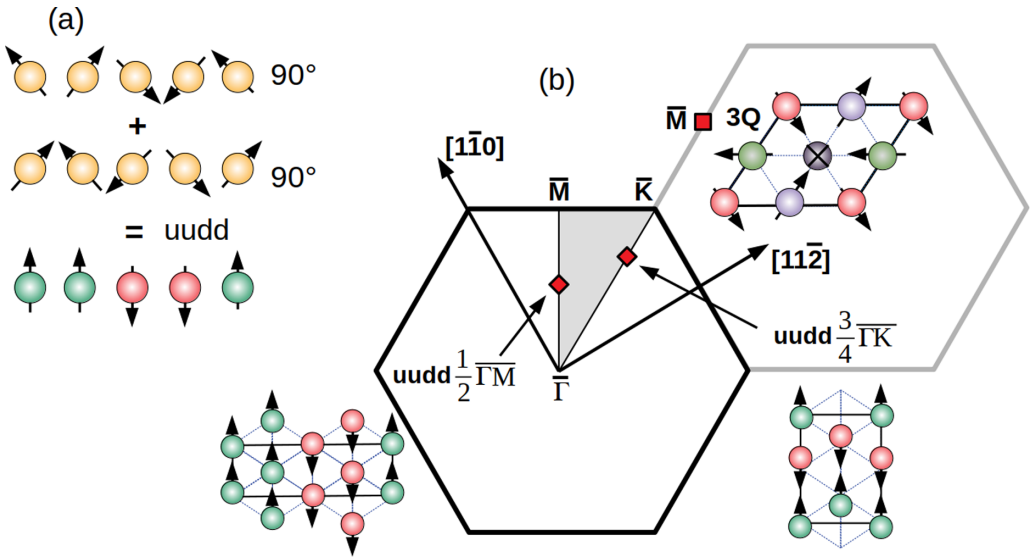

FIG. 2. (a) The superposition of two 90° spin spirals with opposite rotational sense leads to the formation of a collinear *uudd* state. (b) Sketch of the two-dimensional hexagonal Brillouin zone with the position of $\mathbf{q}$ vectors for 90° spin spirals forming the two possible *uudd* states at $\mathbf{q} = \pm\frac{1}{2}\overline{\Gamma\mathrm{M}}$ and $\mathbf{q} = \pm\frac{3}{4}\overline{\Gamma\mathrm{K}}$. The collinear spin structures within their respective unit cells used for our calculations are also depicted besides the position of the three-dimensional $3Q$ state which results from a superposition of $\mathbf{q}$ vectors at three different $\overline{\mathrm{M}}$ points.

linear combination of three orthogonal symmetry equivalent $1Q$ states at the $\overline{\mathrm{M}}$ point of the hexagonal BZ [Fig. 2(b)].

Within the classical Heisenberg model these three multi-Q states are energetically degenerate with their corresponding $1Q$ spin spiral states. This degeneracy is lifted by the HOI terms which can couple the single $1Q$-modes to form the superposition states. Keeping this fact in mind, one can calculate the exchange parameters beyond pairwise Heisenberg exchange within the NN approximation by solving a system of three coupled equations [3]:

$$\Delta E_{\overline{\mathrm{M}}} = E_{3\mathrm{Q}} - E_{\overline{\mathrm{M}},1\mathrm{Q}} = \tfrac{16}{3}(2K_1 + B_1 - Y_1) \tag{2}$$

$$\Delta E_{\frac{1}{2}\overline{\Gamma\mathrm{M}}} = E_{uudd,\frac{\overline{\mathrm{M}}}{2}} - E_{\frac{\overline{\mathrm{M}}}{2},1\mathrm{Q}} = 4(2K_1 - B_1 - Y_1) \tag{3}$$

$$\Delta E_{\frac{3}{4}\overline{\Gamma\mathrm{K}}} = E_{uudd,\frac{3\overline{\mathrm{K}}}{4}} - E_{\frac{3\overline{\mathrm{K}}}{4},1\mathrm{Q}} = 4(2K_1 - B_1 + Y_1). \tag{4}$$

The respective four-atomic unit cells per layer from which both the total energies of the *uudd* states, $E_{uudd,\frac{\overline{\mathrm{M}}}{2}}$ and $E_{uudd,\frac{3\overline{\mathrm{K}}}{4}}$, as well as the energy of the $3Q$ state, $E_{3\mathrm{Q}}$, can be calculated via DFT are sketched in Fig. 2(b) as insets. Here, $E_{\overline{\mathrm{M}},1\mathrm{Q}}$, $E_{\frac{\overline{\mathrm{M}}}{2},1\mathrm{Q}}$, and $E_{\frac{3\overline{\mathrm{K}}}{4},1\mathrm{Q}}$ denote the respective total energy of the corresponding single-Q state. Inverting Eqs. (2)–(4) yields a direct way of calculating the NN HOI terms according to:

$$B_1 = \tfrac{3}{32}\Delta E_{\overline{\mathrm{M}}} - \tfrac{1}{8}\Delta E_{\frac{1}{2}\overline{\Gamma\mathrm{M}}} \tag{5}$$

$$Y_1 = \tfrac{1}{8}\left(\Delta E_{\frac{3}{4}\overline{\Gamma\mathrm{K}}} - \Delta E_{\frac{1}{2}\overline{\Gamma\mathrm{M}}}\right) \tag{6}$$

$$K_1 = \tfrac{3}{64}\Delta E_{\overline{\mathrm{M}}} + \tfrac{1}{16}\Delta E_{\frac{3}{4}\overline{\Gamma\mathrm{K}}}. \tag{7}$$

At this point it must be mentioned that these parameters alter the first three Heisenberg exchange constants obtained from fitting the DFT energy dispersion of spin spirals since their energy contribution to $E(\mathbf{q})$ has the same functional form, e.g., for instance B_1 and J_3 cannot be specified separately from each other. Typically, the J_i are obtained by fitting the DFT spin spiral energy dispersions by only the first term of Eq. (1), i.e., only the Heisenberg exchange. If the full spin model given by Eq. (1) is to be applied, i.e., if the higher-order terms are included, then the first three of the J_i need to be replaced by the modified values J_i' given by [15]:

$$J_1' = J_1 - Y_1 \tag{8}$$

$$J_2' = J_2 - Y_1 \tag{9}$$

$$J_3' = J_3 - \tfrac{1}{2}B_1. \tag{10}$$

In contrast to Y_1 and B_1, the four-site four spin term K_1 yields a constant value of $-12K_1$ for all spin spirals independent of $\mathbf{q}$ and hence does not influence the obtained exchange constants. The modification according to Eqs. (8)–(10) has to be taken into account for further simulations based on the atomistic spin model such as spin dynamics or Monte-Carlo simulations.

B. Computational methods

We have performed DFT calculations within the framework of the all-electron full-potential linearized augmented planewave (FLAPW) method [24–26] as implemented in the FLEUR code [17] and the projector augmented wave (PAW) method [27,28] based on the pseudopotential approach as incorporated in the VASP code [18,29]. We used the local density approximation (LDA) with the interpolation proposed by Vosko, Wilk and Nusair (VWN) [30] to include exchange-correlation effects. We have used LDA in our calculations as it has been used successfully to explain the magnetic ground states observed experimentally in several ultrathin-film systems [8,9,13,14,31]. Similar trends of the magnetic ground state in Fe monolayers on transition metal surfaces have been reported by Hardrat *et al.* using GGA [10]. For all trilayer and film systems we have chosen the theoretical LDA in-plane lattice constant of Ir, i.e., $d_{\mathrm{Ir}} = 2.70$ Å [32], since the starting point of our investigation is the film system Rh/Fe/Ir(111) studied previously [13]. In order to obtain trends from our trilayer calculations which reflect only the change of the transition metal elements we also kept the interlayer distances fixed and as determined for Rh/Fe/Ir(111) (see Table I).

TABLE I. Overview of the in-plane lattice constants and the relaxed interlayer distances from the respective film calculations for all trilayer systems investigated in this paper. The theoretical in-plane lattice constant of Ir is taken from Ref. [32], the in-plane lattice constant of Rh from Ref. [33], relaxed interlayer distances for Fe based trilayers from Ref. [13], and for Co based trilayers from Ref. [16]. For symmetric $4d$/Fe/$4d$ systems the unrelaxed interlayer distance of Rh bulk has been used. All values are given in Å.

	d_{Ir}	$d_{4d\text{-Fe}}$	$d_{\mathrm{Fe\text{-}Ir}}$
fcc-$4d$/Fe/Ir	2.70	1.97	2.07
hcp-$4d$/Fe/Ir	2.70	1.97	2.06
	d_{Ir}	$d_{5d\text{-Fe}}$	$d_{\mathrm{Fe\text{-}Rh}}$
fcc-$5d$/Fe/Rh	2.70	1.97	2.07
	d_{Rh}	$d_{4d\text{-Fe}}$	$d_{\mathrm{Fe\text{-}}4d}$
fcc-$4d$/Fe/$4d$	2.72	2.22	2.22
	d_{Ir}	$d_{4d\text{-Co}}$	$d_{\mathrm{Co\text{-}Ir}}$
fcc-$4d$/Co/Ir	2.70	2.06	2.15

For the trilayers we only change the $4d$ or $5d$ element, while the geometric structure is kept fixed. Besides Rh as a $4d$ transition metal we consider Tc, Ru, and Pd along the row of the periodic table, whereas the $5d$ element Ir is replaced by Re, Os, and Pt. In a similar fashion the relaxed interlayer distances from Rh/Co/Ir(111) [16] serve as a starting point to calculate the exchange parameters for Co based trilayers. In addition, the properties of symmetric $4d$/Fe/$4d$ systems have been evaluated based on the in-plane lattice constant of Rh which amounts to 2.72 Å and the unrelaxed interlayer distances of bulk Rh (see Table I).

The spin spiral energy dispersions and total energies of the collinear *uudd* states have been calculated via the FLAPW method for all Fe and Co based trilayers. Using the generalized Bloch theorem [24] total energies of flat spin spirals can be computed self-consistently in the chemical unit cell within the scalar-relativistic approximation. We have used 1936 k points in the full 2D BZ and a large cutoff of $k_{\mathrm{max}} = 4.1$ a.u.$^{-1}$ to ensure convergence with the basis function set. The muffin tin radii have been chosen as 2.31 a.u. for both $4d$ and $5d$

elements, while a slightly smaller value of 2.23 a.u. has been set for the magnetic elements Fe and Co. For the *uudd* states only the number of k points has been adapted in such a way that its density in the full 2D BZ corresponds approximately to that used for the respective spin spiral calculation; hence, the k-point set amounts to 168 in the irreducible part of the first BZ for the *uudd* state along $\overline{\Gamma M}$ and to 336 for the *uudd* state along the $\overline{\Gamma K}$ direction.

For Co based trilayers the energy differences between the $3Q$ and the RW-AFM state have been calculated by the FLAPW method within the four-atomic unit cell per layer as well; here, 484 k points in the full 2D BZ have been chosen which is exactly one quarter of the number of k points used for the respective spin spiral calculation.

For the Fe based trilayers [and the Rh/Fe/Rh(111) film system] the energy differences between the $3Q$ and the RW-AFM state have been calculated using the PAW method. A $28 \times 28 \times 1$ $\overline{\Gamma}$-centered $(15 \times 15 \times 1)$ k-point mesh and the standard energy cutoffs as supplied by the respective potential file library of VASP have been used. In Appendix A we demonstrate that mixing both DFT methods in this way is a valid procedure for obtaining trends of HOI parameters in Fe based transition metal trilayers and film systems by applying convergence tests to selected systems.

We have also determined the HOI parameters for selected film systems. As discussed in the previous section, we need the energy dispersion $E(\mathbf{q})$ of spin spirals as well as the total energies of the three multi-Q states. For the film systems Pd/Fe/Ir(111), Rh/Fe/Ir(111), and Rh/Co/Ir(111) we have used $E(\mathbf{q})$ from our previous work [13,16,32]. For these systems we have calculated for both stackings of the Pd or Rh overlayer via FLEUR the missing multi-Q states with the same setup of the films as in the cited references. For Pd/Fe/Ir(111) and Rh/Co/Ir(111), we have calculated the $3Q$ and the two *uudd* states, while only the $3Q$ state was required for Rh/Fe/Ir(111), since both *uudd* states have been calculated previously [13]. For fcc- and hcp-Rh/Fe/Rh(111), we have calculated $E(\mathbf{q})$ and the two *uudd* states using FLEUR. The total energy difference between the RW-AFM and the $3Q$ state has been obtained using VASP. Asymmetric films with nine Rh layers have been used for all calculations and the film structure was relaxed. For fcc-Pd/Co/Ir(111), we have calculated $E(\mathbf{q})$ and all three multi-Q states using FLEUR. Asymmetric films with nine Ir layers have been used for all calculations and the film structure was relaxed [34]. For all multi-Q state calculations we used the same k-point meshes as for the freestanding trilayers and a value of $k_{\max} = 4.1$ a.u.$^{-1}$.

III. RESULTS AND DISCUSSION

A. Fe based trilayers

We start our discussion with the trend of Heisenberg exchange and HOI parameters for symmetric $4d$/Fe/$4d$ trilayers. In these systems, the effect of the band filling in the $4d$ layer on the magnetic properties of the Fe layer is already clearly revealed. Note that our trilayers are element-wise and structurally symmetric since we use the same $4d$-Fe distance for both interfaces (see Table I). These results also facilitate to understand the trends for the more complex asymmetric trilayers $4d$/Fe/Ir and $5d$/Fe/Rh. Note that these trilayers are isoelectronic if we use the $4d$ and $5d$ transition metal with the same number of d electrons. The reference system for these trilayers is Rh/Fe/Ir. For the corresponding ultrathin film system Rh/Fe/Ir(111) a stacking-dependent change of the magnetic ground state has been observed [13]. Therefore, we consider both fcc- and hcp-stacking of $4d$/Fe/Ir trilayers. Finally, we compare the trends from the trilayers with experimental and theoretical results for the corresponding ultrathin film systems.

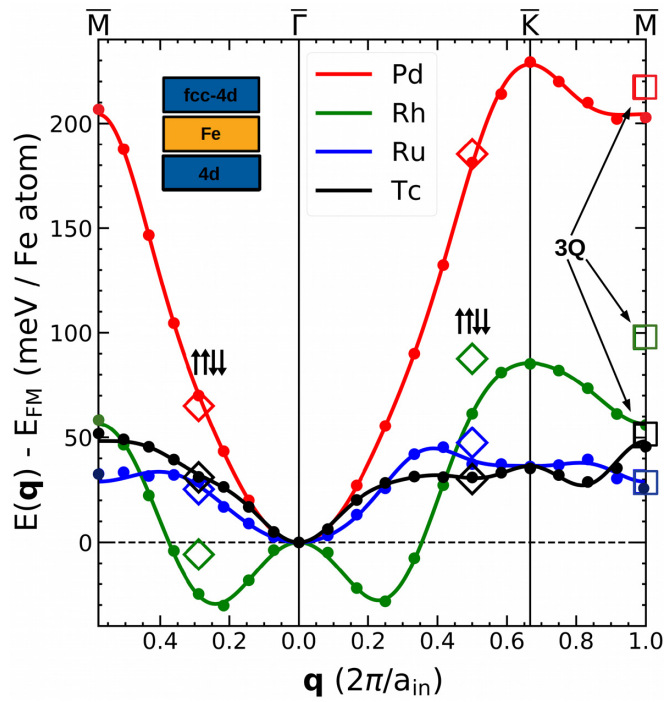

FIG. 3. Energy dispersion of flat spin spirals for symmetric fcc-$4d$/Fe/$4d$ trilayers. Total energies calculated by DFT are marked by filled circles, whereas the solid lines represent fits to the Heisenberg model. Both energies of the *uudd* ($\uparrow\uparrow\downarrow\downarrow$) states as well as the $3Q$ state are plotted as empty diamonds and squares at the q values of the corresponding single-Q states, respectively. a_{in} denotes the in-plane lattice constant.

1. Symmetric 4d/Fe/4d trilayers

We begin with the energy dispersion $E(\mathbf{q})$ of flat spin spirals in symmetric $4d$/Fe/$4d$ trilayers in fcc stacking along both high symmetry directions of the hexagonal 2D BZ (Fig. 3). The energy dispersion of Pd/Fe/Pd is characteristic for a system dominated by a nearest-neighbor ferromagnetic exchange interaction. The FM state at the $\overline{\Gamma}$ point exhibits the lowest energy and the dispersion rises quickly for spin spirals with increasing $\mathbf{q}$, i.e., decreasing spin spiral period. The RW-AFM state at the $\overline{\mathrm{M}}$ point and the Néel state at the $\overline{\mathrm{K}}$ point are more than 200 meV/Fe atom higher than the FM state. For Rh/Fe/Rh, the energy dispersion is qualitatively different: The RW-AFM state and the Néel state have decreased in energy and spin spiral energy minima occur along both high symmetry directions. The energy dispersions of Ru/Fe/Ru and Tc/Fe/Tc look similar with the FM state being lowest

TABLE II. Magnetic moments of the symmetric fcc-4*d*/Fe/4*d* trilayers for the ferromagnetic state. All values are given in μ_B.

4*d*/Fe/4*d*	m_{4d}	m_{Fe}	m_{4d}
Tc/Fe/Tc	−0.08	+2.20	−0.08
Ru/Fe/Ru	−0.35	+2.34	−0.35
Rh/Fe/Rh	+0.33	+3.02	+0.33
Pd/Fe/Pd	+0.30	+3.05	+0.30

but small energy differences with respect to the states at the zone boundaries.

In Fig. 3 the energies of the three multi-Q states with respect to the FM state are shown at the **q** vectors of the corresponding single-Q states. For Fe trilayers with Pd, Ru, and Tc overlayers, the multi-Q states are energetically relatively close to the spin spiral energy dispersion. However, for Rh/Fe/Rh the multi-Q states are quite far from the respective spin spiral energies, by about 20 to 40 meV/Fe atom, indicating a significant contribution of higher-order exchange interactions. However, in none of the fcc-4*d*/Fe/4*d* trilayers a multi-Q state is the energetically lowest magnetic structure. As shown in Fig. 12 in Appendix C, the situation changes upon choosing the hcp stacking sequence for Rh/Fe/Rh: Now the *uudd* state along the $\overline{\Gamma M}$ direction turns out to be the state of lowest energy.

The magnetic moments of both the Fe layer and the adjacent 4*d* layers are listed in Table II. Since the geometric structure is the same for all trilayers, the change of the magnetic moment in the Fe layer arises only due to the 3*d*-4*d* hybridization. Two effects play a role. First, the 4*d* band in the adjacent layers moves to lower energies which modifies the hybridization with the Fe 3*d* bands. Second, the extent of the 4*d* orbitals decreases with increasing nuclear number due to the imperfect screening of the nuclear Coulomb potential by the 4*d* electrons. This leads to a decrease of overlap with the 3*d* Fe states. As a result of both effects the Fe magnetic moment rises with 4*d* band filling. The induced magnetic moments in the adjacent 4*d* layers can be quite considerable due to the large spin susceptibility of the 4*d* transition metals which also leads to the AFM alignment at the beginning of the series, for Tc and Ru, and FM ordering at the end of the series, for Rh and Pd.

From fitting the DFT energy dispersions of spin spirals shown in Fig. 3 the pairwise Heisenberg exchange constants are obtained. Figure 4(a) shows the trend of the exchange constants for fcc-4*d*/Fe/4*d* trilayers up to the third nearest neighbor without modification by HOI terms. The NN exchange constant J_1 rises nearly linearly from Ru/Fe/Ru to Pd/Fe/Pd in accordance with the increasing energy difference between the FM state and the RW-AFM state seen in Fig. 3. For Tc/Fe/Tc and Ru/Fe/Ru all exchange constants are similar in agreement with the similar energy dispersions. In addition, J_2 and J_3 of Tc/Fe/Tc and Ru/Fe/Ru are on the same order of magnitude as J_1 leading to a remarkable flattening of their spin spiral curves as compared to Pd/Fe/Pd.

From Ru/Fe/Ru to Rh/Fe/Rh a change of sign of J_2 and J_3, i.e., preferred AFM coupling, is observed which leads to exchange frustration in the latter trilayer and the spin spiral minima seen in Fig. 3. Although J_2 and J_3 mediate an AFM coupling in the case of Pd/Fe/Pd as well, the system is not dominated by exchange frustration since the FM NN exchange constant J_1 is by a factor of eight larger. Instead, as already stated above, the energy dispersion shows a prototypical FM behavior. We have also calculated spin spiral energy dispersions for the hcp stacking of Rh/Fe/Rh (see Fig. 12 in Appendix C). As seen in Fig. 4(a), J_1 decreases by about 4 meV and J_2 is reduced by a factor of two. This is due to an energy dispersion with only shallow spin spiral minima (cf. Fig. 12 in Appendix C) .

The trend of the exchange interactions in the trilayers is consistent with DFT calculations for Fe monolayers (MLs) on fcc(111) and hcp(0001) surfaces of 4*d* and 5*d* transition metals [10]. In that work, it has been reported that there is a transition from AFM coupling for Fe MLs in hcp stacking on Tc(0001) and Re(0001) to FM coupling for Fe MLs in fcc stacking on Pd(111) and Pt(111), i.e., an increase of J_1 with *d* band filling. Due to the fcc stacking our trilayers do not show AFM nearest-neighbor coupling at the beginning of the series. Nevertheless, the same explanation for the behavior of J_1 holds as reported in Ref. [10]: the observed trend is a result of the hybridization between the 3*d* bands of Fe and the 4*d*

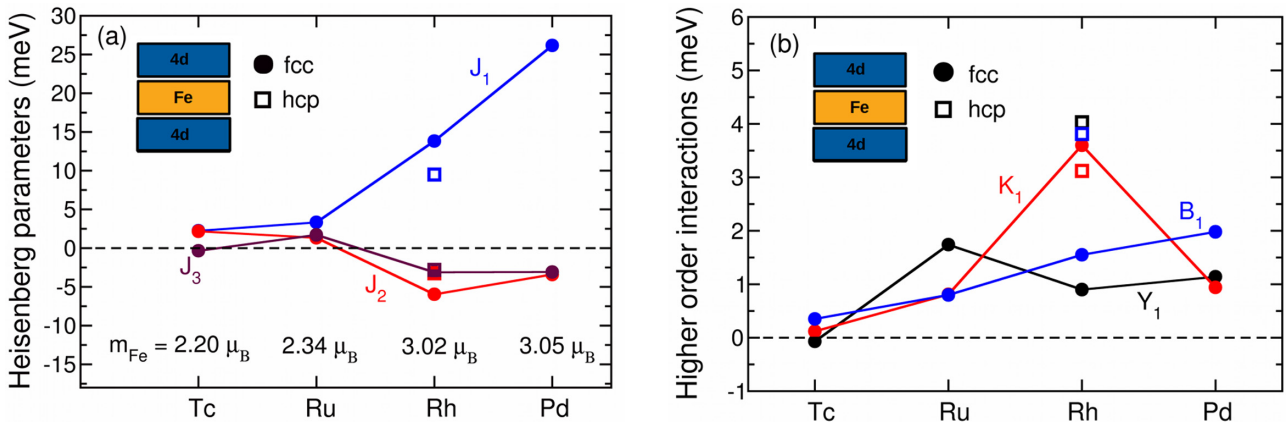

FIG. 4. Comparison of the trend for (a) the Heisenberg exchange constants as extracted from fitting the corresponding spin spiral dispersions, i.e., without modification by HOI terms, and (b) the HOI parameters for symmetric 4*d*/Fe/4*d* trilayers. The lines connecting the data points serve as a guide to the eye.

TABLE III. Magnetic moments of the asymmetric Fe based trilayers for the ferromagnetic state. All values are given in μ_B.

$4d$/Fe/Ir	m_{4d}	m_{Fe}	m_{Ir}
Tc/Fe/Ir	−0.21	+1.70	+0.08
Ru/Fe/Ir	−0.26	+1.75	−0.03
Rh/Fe/Ir	+0.23	+2.43	−0.00
Pd/Fe/Ir	+0.37	+2.81	+0.09
$5d$/Fe/Rh	m_{5d}	m_{Fe}	m_{Rh}
Re/Fe/Rh	−0.14	+2.11	+0.42
Os/Fe/Rh	−0.24	+1.93	+0.20
Ir/Fe/Rh	−0.00	+2.43	+0.23
Pt/Fe/Rh	+0.30	+2.89	+0.38

bands of the nonmagnetic adjacent layers which is changed with increasing filling of electrons. This altering $3d$-$4d$ hybridization also becomes apparent in the increasing magnetic Fe moments along the investigated series [see Fig. 4(a)].

The HOI constants for the fcc-$4d$/Fe/$4d$ trilayers are shown in Fig. 4(b). It is apparent that the biquadratic term rises with increasing $4d$ band filling as the NN exchange constant. In contrast, the trend of the four-site four spin interaction displays a striking maximum for Rh/Fe/Rh trilayers. The three-site four spin interaction is of similar magnitude as the biquadratic term and follows a trend more similar to the third-nearest neighbor exchange. The HOI constants are smaller than J_1 in all cases, however, they can be of similar or even larger value compared to the second and third-nearest neighbor exchange. For Ru/Fe/Ru the values of the pairwise and higher-order exchange constants are quite comparable.

For an hcp stacking of the Rh/Fe/Rh trilayer, the biquadratic and three-site four spin interactions are drastically enhanced to values of about 3.8 and 4.0 meV, respectively, and even exceed the value of K_1 [Fig. 4(b)]. K_1 is slightly smaller by 0.7 meV than in the fcc case. Hence, there is a significant effect of the stacking order on the higher-order exchange interactions while the pairwise exchange interactions are much less sensitive to the stacking sequence. As a result the *uudd* state along the $\overline{\Gamma\mathrm{M}}$ direction is the magnetic ground state of the hcp-Rh/Fe/Rh trilayer (see Fig. 12 in Appendix C). We find a change of the magnetic ground state from a spin spiral for fcc Rh stacking to the *uudd* state for hcp stacking also for the corresponding film system Rh/Fe/Rh(111) (HOI values are given in Table IV).

TABLE IV. Higher-order exchange constants K_1, B_1, and Y_1 for ultrathin film systems. Values for HOI parameters of fcc-Fe/Ir(111) and hcp-Fe/Rh(111) are taken from Ref. [12]. All values are given in meV.

Film system	K_1	B_1	Y_1
fcc-Rh/Fe/Ir(111)	2.48	3.33	−0.85
hcp-Rh/Fe/Ir(111)	1.88	4.14	3.84
fcc-Pd/Fe/Ir(111)	2.79	3.38	2.15
hcp-Pd/Fe/Ir(111)	2.41	1.57	2.15
fcc-Rh/Fe/Rh(111)	3.18	2.79	1.11
hcp-Rh/Fe/Rh(111)	2.48	5.88	5.12
fcc-Fe/Ir(111)	−1.28	−0.24	−0.24
hcp-Fe/Rh(111)	0.10	3.40	4.00
fcc-Rh/Co/Ir(111)	−0.58	1.79	−0.96
hcp-Rh/Co/Ir(111)	−1.01	0.34	−1.55
fcc-Pd/Co/Ir(111)	−1.41	1.60	−1.39

2. $4d$/Fe/Ir *and* $5d$/Fe/Rh *trilayers*

Now we turn to asymmetric Fe based trilayers. Since the starting point of our study is the film system Rh/Fe/Ir(111),

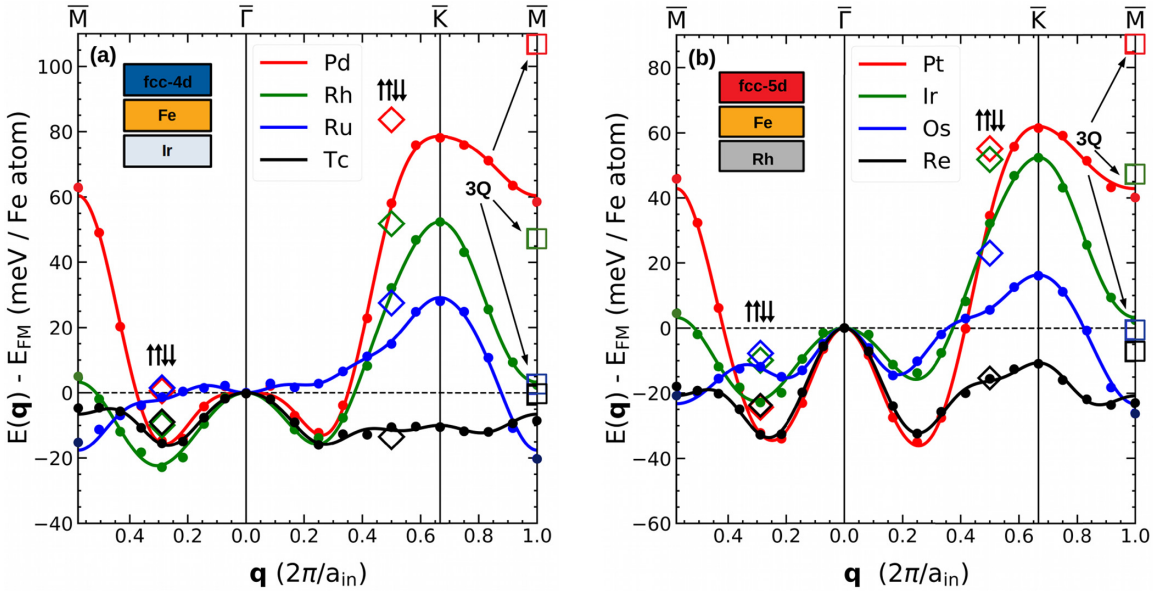

FIG. 5. Energy dispersion of flat spin spirals for (a) fcc-$4d$/Fe/Ir and (b) fcc-$5d$/Fe/Rh trilayers. Total energies calculated by DFT are marked by filled circles, whereas the solid lines represent fits to the Heisenberg model. Both energies of the *uudd* ($\uparrow\uparrow\downarrow\downarrow$) states as well as the $3Q$ state are plotted as empty diamonds and squares at the q values of the corresponding single-Q states, respectively.

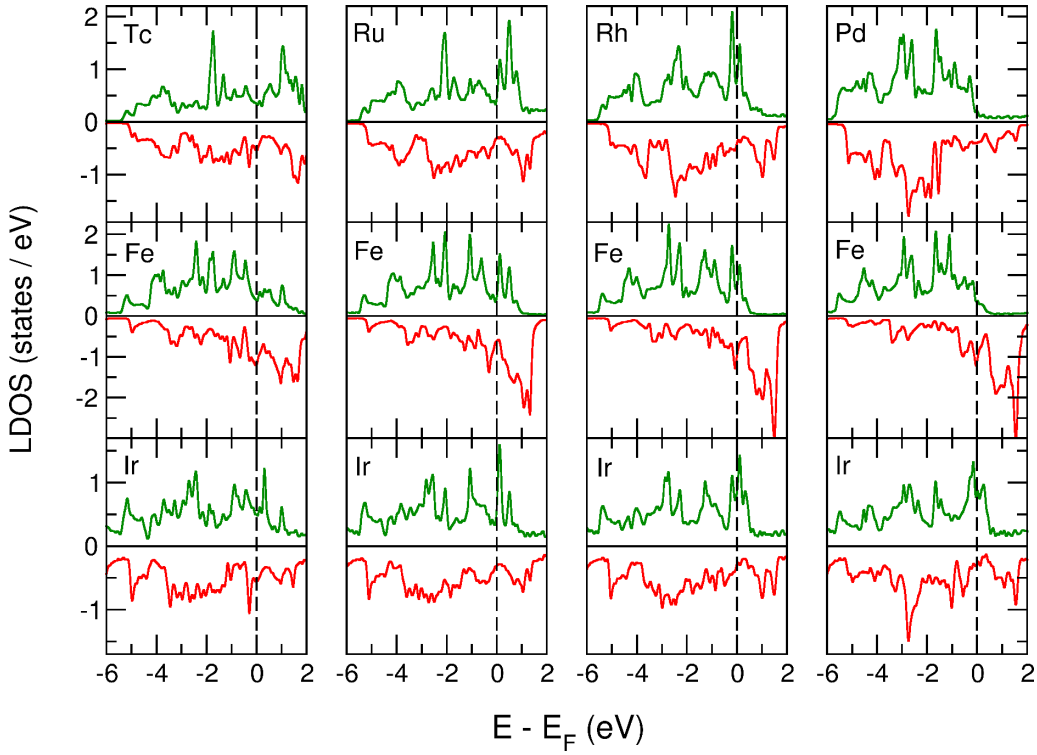

FIG. 6. Local density of states (LDOS) of the fcc-4d/Fe/Ir trilayers in the ferromagnetic state. The upper panels show the LDOS of the 4d overlayer, the middle panels the LDOS of the Fe layer, and the lower panels that of the Ir layer. Majority and minority spin channels are represented in green and red color, respectively.

we consider 4d/Fe/Ir trilayers. In order to investigate the effect of isoelectronic 4d vs. 5d transition metals, we have further performed calculations for 5d/Fe/Rh trilayers. Figure 5 shows the energy dispersions of flat spin spirals for these two types of trilayers. The most striking feature for all systems except those with Ru and Os are the deep energy minima along both high symmetry directions of the BZ. The values of $\mathbf{q}$ for these minima correspond to a period of about $\lambda \approx 1.0$ nm. They are close to those found in the energy dispersion of the symmetric Rh/Fe/Rh trilayer (cf. Fig. 3). This is a result of the strong effect of the hybridization at the Fe/Rh or the isoelectronic Fe/Ir interface which clearly dominates the energy dispersion.

For the 4d/Fe/Ir trilayers the spin spiral minima are relatively similar in depths up to 23 meV/Fe atom below the FM state, while for 5d/Fe/Rh trilayers the minima are deepest with a maximum value of about 35 meV/Fe atom below the FM state for the case of a Re and Pt overlayer. For Ru/Fe/Ir and Os/Fe/Rh, the row-wise antiferromagnetic state ($\overline{\mathrm{M}}$ point) is the ground state, while all other trilayers possess a spin spiral energy minimum. Both types of ground states indicate competing exchange interactions. As it can be seen from Fig. 5 as well, the *uudd* states and the 3Q state are higher in energy than the corresponding single-Q (spin spiral) states in these systems. The only exception is the Tc/Fe/Ir trilayer for which the *uudd* state along the $\overline{\Gamma\mathrm{K}}$ direction is below the respective spin spiral state.

The Fe atoms in all trilayers exhibit a nearly constant magnetic moment independent of $\mathbf{q}$. Our DFT calculations reveal only small deviations of about 6% from the magnetic moments of the FM state (see also Table III). Hence they are, to a good approximation, independent of the spin state and fulfill the basic condition of the Heisenberg model. In contrast, the moments of Ru/Fe/Ir and its isoelectronic counterpart Os/Fe/Rh show differences of up to 17% from the FM state which necessitates the inclusion of the Stoner energy term in order to fit the DFT data (Fig. 5). Therefore, the calculated energies of these two trilayers have been shifted by $\frac{1}{2}I(M(q) - M(0))^2$ with I being the Stoner parameter (420 meV for Fe [35]) and $M(0)$ denoting the magnetic moment of Fe at the $\overline{\Gamma}$ point.

The varied hybridization due to the band filling of the overlayer can be seen in the local density of states shown for the example of 4d/Fe/Ir trilayers in Fig. 6. As we move through the 4d series from Tc to Pd, the Fermi energy moves from the center to the end of the 4d bands (upper panels of Fig. 6). This shift of the 4d band affects strongly the 3d LDOS of the Fe layer (middle panels of Fig. 6). In particular, the majority spin channel displays large changes in the vicinity of the Fermi energy. Thereby, the exchange interactions are significantly modified which is manifested in the spin spiral energy dispersions discussed above. The reduced magnetic moment of the Fe layer for trilayers (cf. Table III) with an overlayer from the beginning of the 4d series can also be understood based on the variation of the majority spin LDOS. A similar effect as shown for the 4d/Fe/Ir trilayers in Fig. 6 is found for the 5d/Fe/Rh and the 4d/Fe/4d trilayers (not shown).

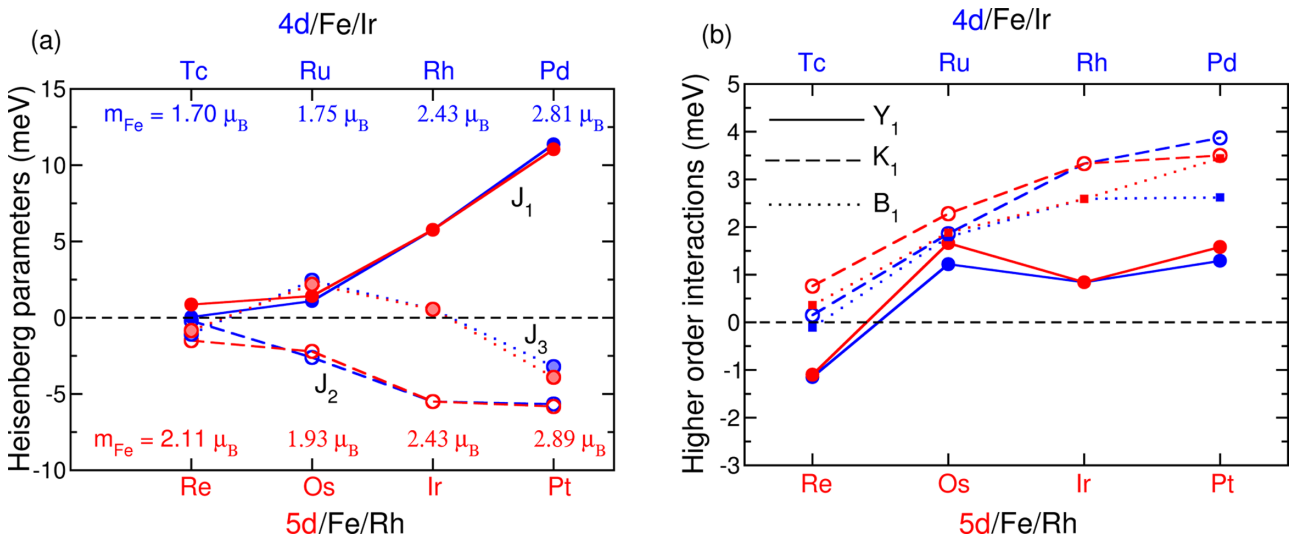

FIG. 7. Trends for fcc-4d/Fe/Ir and fcc-5d/Fe/Rh trilayers for both (a) Heisenberg exchange constants up to the third nearest neighbor as extracted from fitting the corresponding spin spiral dispersions, i.e., without modification by HOI terms, and (b) HOI parameters Y_1 (solid line), K_1 (dashed line), and B_1 (dotted line) for isoelectronic Fe based trilayers in fcc stacking. The lines connecting the data points serve as a guide to the eye. Blue (red) color denotes 4d/Fe/Ir (5d/Fe/Rh) trilayers.

From the energy dispersions of Fig. 5 one can evaluate trends for both the Heisenberg and higher-order exchange interactions of these Fe based trilayers. First we focus on the pairwise exchange constants shown in Fig. 7(a). We find that the nearest-neighbor constant J_1 rises with an increasing number of electrons in the 4d as well as in the 5d shell. The trend is very similar to that observed already for the symmetric 4d/Fe/4d trilayers, however, the magnitude of J_1 is much reduced. This is also a result of the stronger hybridization since we have used the relaxed interlayer distances for the asymmetric trilayers (cf. Table I). For the isoelectronic 4d/Fe/Ir and 5d/Fe/Rh trilayers the values of J_1 are quite similar and follow the same trend.

The same is true for the next-nearest and third-nearest neighbor constant J_2 and J_3, respectively. However, their qualitative trend is considerably different as compared to the one found for J_1. While J_1 mediates a FM coupling between nearest neighbors in all cases, J_2 displays an AFM behavior throughout the whole series and J_3 even experiences a change of sign as one goes from Tc to Ru (Rh to Pd) and the respective isoelectronic counterparts. These findings support our conclusion from the energy dispersions, namely that one is dealing with largely exchange frustrated systems. It is also clear from Fig. 7(a) that the values for the NN constant J_1 span a larger order of magnitude ranging up to about 11 meV for Pd/Fe/Ir than for J_2 and J_3 which only exhibit a variation of 5 to 6 meV.

We now turn to the HOI parameters of isoelectronic Fe based trilayers [Fig. 7(b)] calculated from the energy differences between multi-Q and the respective spin spiral states according to Eqs. (5)–(7). One sees a slightly different trend than for the Heisenberg exchange constants. The three-site four spin term Y_1 first rises moving from Tc/Fe/Ir (Re/Fe/Rh) to Ru/Fe/Ir (Os/Fe/Rh) thereby experiencing additionally a change of sign before remaining nearly constant at $\approx$1 meV for the rest of the series. Here, the qualitative behavior is observed to be the same for 4d/Fe/Ir and 5d/Fe/Rh trilayers as well. In contrast, both the biquadratic and four-site four spin term only exhibit positive values (except for Tc/Fe/Ir) which rise with increasing d band filling [Fig. 7(b)]. Additionally, both display higher maximum values of up to about 3.9 meV for Pd/Fe/Ir than for Y_1 which peaks at 1.7 meV for Os/Fe/Rh.

3. *Effect of stacking sequence*

Next we take a look at the influence of varying the stacking sequence of the atomic layers upon both the Heisenberg exchange and HOI parameters. This effect is investigated for the example of the 4d/Fe/Ir trilayer series and the corresponding ultrathin film systems Rh/Fe/Ir(111) and Pd/Fe/Ir(111) which have been studied experimentally [13,36–39]. The energy dispersion of hcp-4d/Fe/Ir trilayers including the position of multi-Q states is shown in Fig. 13 in Appendix C.

Figure 8 shows the trends of all pairwise and higher-order exchange parameters for fcc- and hcp-4d/Fe/Ir trilayers and the film systems mentioned. As for the fcc-4d/Fe/Ir trilayers [Fig. 8(a)], there is an increase of J_1 with band filling in the adjacent 4d layer [Fig. 8(b)]. However, for the hcp stacked trilayers we find a change of sign of J_1 from Rh/Fe/Ir to Ru/Fe/Ir [40] similar to that observed for Fe monolayers in hcp stacking on Ir(111) [10]. The second and third-nearest neighbor exchange, J_2 and J_3, show the same qualitative behavior for the two types of stacking, i.e., both drop along the series until they mediate an AFM coupling for both fcc- and hcp-Pd/Fe/Ir [see Figs. 8(a) and 8(b)]. This effect is slightly smaller for J_2 in the hcp trilayers with values ranging between about 0.4 meV for Ru and -2.0 meV for Pd than in the fcc systems for which this exchange constant spans a larger order of magnitude with about 5.5 meV. The opposite is true for J_3 whose values vary over a range of more than 9 meV for the case of hcp stacking as compared to fcc-4d/Fe/Ir trilayers with a considerably smaller range of about 5.6 meV. In particular, for hcp-Ru/Fe/Ir J_1 and J_3 are of nearly the same absolute value but opposite sign.

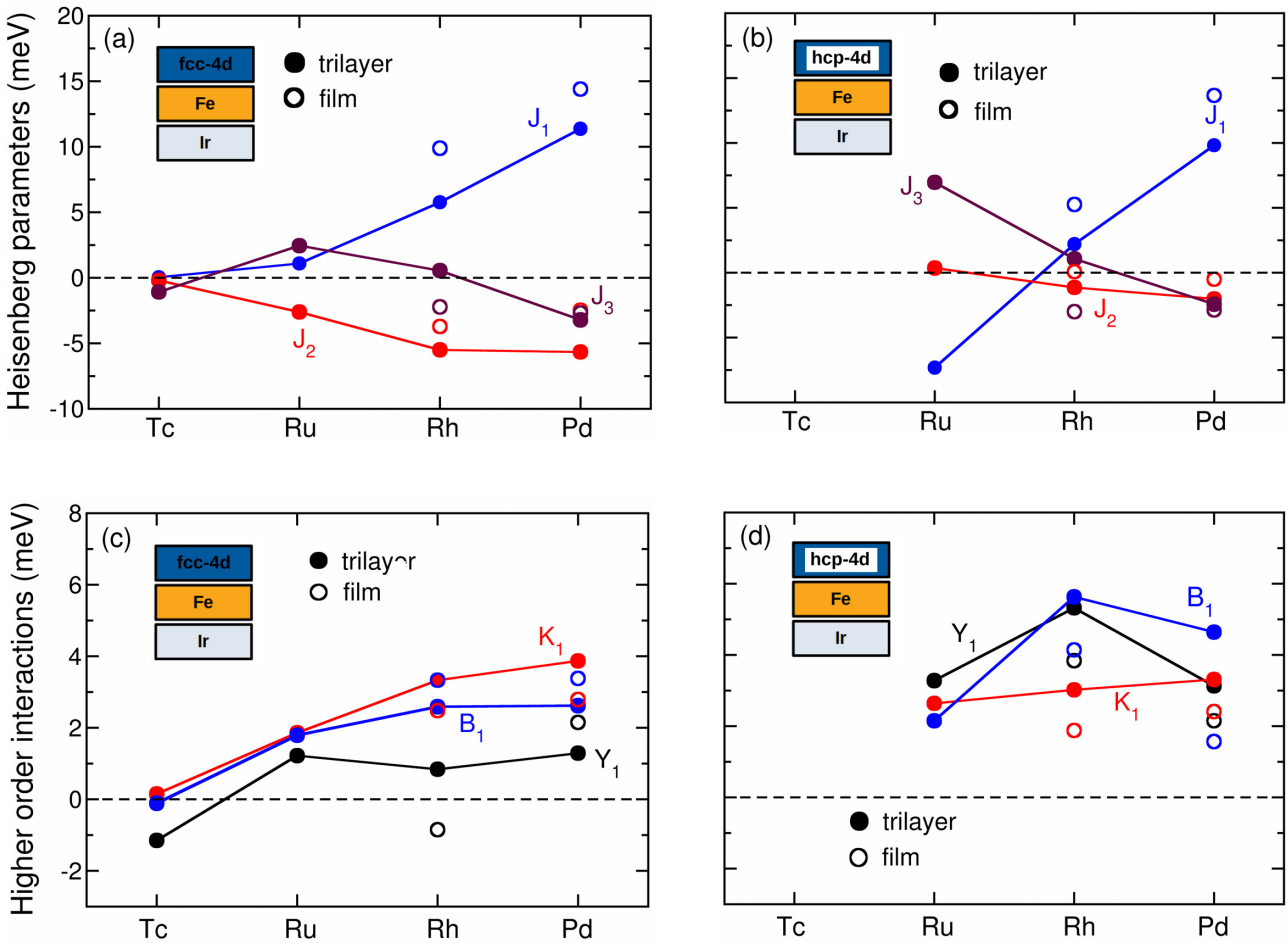

FIG. 8. Trend of (a,b) the first three Heisenberg exchange parameters as extracted from fitting the corresponding spin spiral dispersions, i.e., without modification by HOI terms and (c,d) the HOI parameters for fcc- and hcp-4*d*/Fe/Ir trilayers (filled circles) as well as for the corresponding film systems Rh/Fe/Ir(111) and Pd/Fe/Ir(111) (open circles). The lines connecting the data points serve as a guide to the eye.

Figures 8(c) and 8(d) reveal a qualitatively different behavior for the HOI parameters of hcp and fcc trilayers. Especially the biquadratic and the three-site four spin terms, B_1 and Y_1, exhibit larger values in hcp stacking throughout the series. In addition, they also show a striking maximum of about 5.6 meV and 5.3 meV, respectively, for hcp-Rh/Fe/Ir. In contrast, K_1 which amounts to a large value of about 3.0 meV turns out to be the smallest HOI term for this trilayer. The large values of B_1 and Y_1 are linked to the *uudd* state along $\overline{\Gamma\mathrm{M}}$ being the ground state of hcp-Rh/Fe/Ir (cf. Fig. 13 in Appendix C). In contrast, a spin spiral ground state was observed for fcc-Rh/Fe/Ir (cf. Fig. 5).

4. Trilayers vs. film systems

Now we compare the trilayer results with those obtained for film systems. Concerning the pairwise exchange constants [Figs. 8(a) and 8(b)], we find that the film systems Rh/Fe/Ir(111) and Pd/Fe/Ir(111) follow the same trend as the corresponding trilayers. This shows that the magnetic exchange interaction in the Fe layer is dominated by the hybridization at the interfaces with the 4*d* and 5*d* transition metal layers. The stacking dependence of the exchange constants is also captured in the trilayer calculations.

The values of the HOI parameters for hcp-Rh/Fe/Ir(111) are slightly lower than for the trilayer, however, they are still larger than both the biquadratic as well as the three spin term for fcc-Rh/Fe/Ir(111) [Figs. 8(c) and 8(d)]. The obtained values of the HOI constants explain the origin of the stacking-dependent magnetic ground state observed by spin-polarized STM [13]. In particular, the change of sign and large increase of the three-site four spin term, Y_1, for hcp-Rh stacking drives the change from the spin spiral for fcc to the *uudd* state along $\overline{\Gamma\mathrm{M}}$ for hcp-Rh stacking [cf. Eq. (3)].

A similar combination of HOI parameters has been reported for hcp-Fe/Rh(111) [12] in which an *uudd* state has been found as magnetic ground state. While K_1 is vanishingly small for this system, both B_1 and Y_1 are on the same order of magnitude with maximum values of 4 meV [12]. The opposite is true for an fcc Fe monolayer on Ir(111) which is known to exhibit a quadratic nanoskyrmion lattice as magnetic ground state induced by the interplay of a strong four-site four spin interaction and the DMI [9]. As calculated in [12], fcc-Fe/Ir(111) is indeed characterized by tiny values of B_1 and Y_1 (see also Table IV), whereas K_1 represents the dominant HOI parameter contrary to both hcp-Fe/Rh(111) as well as hcp-Rh/Fe/Ir(111).

For Pd/Fe/Ir(111) the observed magnetic ground state is a spin spiral for both stackings [36,38]. However, in an applied magnetic field a skyrmion lattice becomes favorable and in the field-polarized state isolated magnetic skyrmions are metastable [32,36]. Recently, it has been shown that the four-site four spin interaction K_1 plays an important role for the stability of skyrmions [15]. For a positive sign of K_1, observed for the Pd/Fe/Ir trilayers and Pd/Fe/Ir(111) films [Figs. 8(c) and 8(d)], the energy barriers stabilizing individual topological spin structures such as skyrmions or antiskyrmions are enhanced by about 40 to 60 times K_1 amounting to a large enhancement for Pd/Fe/Ir(111) [15].

B. Co based trilayers

In this section we investigate the effect of substituting the central magnetic layer by Co, i.e., we study fcc-4d/Co/Ir trilayers. A motivation is the recent observation of magnetic skyrmions in zero magnetic field in atomic Rh/Co bilayers on the Ir(111) surface [16]. On the other hand, for Pd/Co/Ir(111) only ferromagnetic domains have been observed in spin-polarized STM experiments [41]. We start again by discussing the energy dispersion of flat spin spirals for fcc-4d/Co/Ir trilayers before presenting trends for the Heisenberg exchange and HOI parameters of both trilayers and the corresponding film systems for which we have calculated exchange constants and HOI parameters as well.

The energy dispersion of flat spin spirals calculated along both high symmetry directions of the 2D BZ for Co based trilayers is shown in Fig. 9. In contrast to the previously presented Fe based trilayers, exchange frustration effects do not manifest themselves in energy minima of the dispersion [cf. Fig. 5(a)] but rather in very flat $E(\mathbf{q})$ curves around the $\overline{\Gamma}$ point. Furthermore the energy difference between the FM state at the $\overline{\Gamma}$ point and the RW-AFM at the boundary of the BZ is quite large for the Co based trilayers compared to the corresponding 4d/Fe/Ir systems [see Fig. 5(a)] indicating a stronger FM coupling of the nearest neighbors. This becomes most evident for Rh/Co/Ir and Pd/Co/Ir with values of about 200 meV/Co atom (Fig. 9). The same behavior of spin spiral energy dispersions has recently been reported for the ultrathin Rh/Co/Ir(111) film system based on DFT [16] and the trend of 4d/Co/Ir(111) is very similar [34] to that observed in the trilayers.

Figure 9 also shows that the energy differences between the *uudd* states along both high-symmetry directions of the 2D BZ and the corresponding single-Q states are negative in all cases. This observation represents another qualitative difference compared to the Fe based trilayers.

Table V lists both the magnetic moments of the Co atoms as well as the induced moments of the adjacent nonmagnetic 4d and Ir layers in the FM state. As for the 4d/Fe/Ir trilayers (see Table III), our DFT calculations reveal an antiparallel alignment between the induced magnetic moments in the 4d layers and the Co atom for the first half of the series and a parallel alignment for the second half. As expected from Hund's rules, the magnetic moments of the Co atoms turn out to be smaller than the moments in the respective Fe based trilayers. Due to increased 3d-4d hybridization the Co moment is reduced for adjacent layers of 4d elements from the beginning of the series. For example, Co sandwiched between Tc and Ir exhibits the smallest value of 1.07 μ_B, while Co in between Pd and Ir has the largest one with 2.08 μ_B.

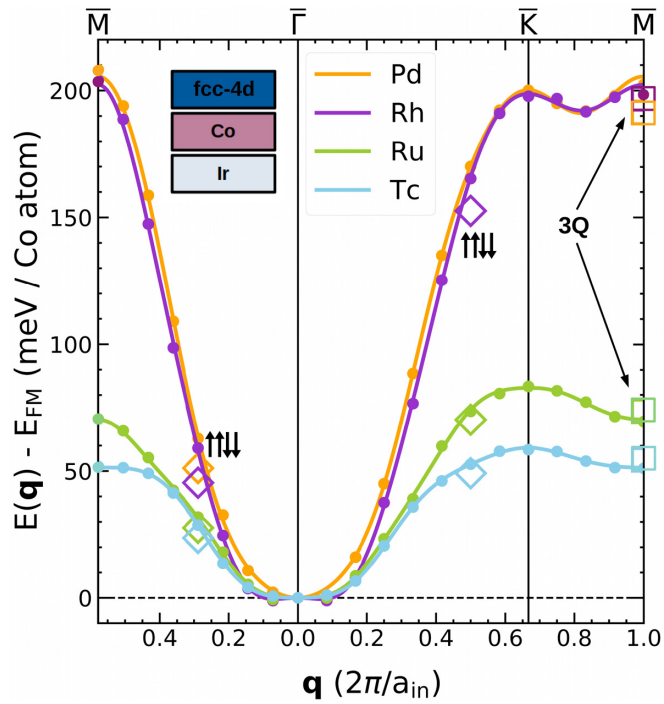

FIG. 9. Energy dispersion of flat spin spirals for fcc-4d/Co/Ir trilayer systems. Total energies calculated by DFT are marked by filled circles, whereas the solid lines represent fits to the Heisenberg model. Both energies of the *uudd* (↑↑↓↓) states as well as the 3Q state are plotted as empty diamonds and squares at the q values of the corresponding single-Q states, respectively.

The spin-resolved local density of states for the 4d/Co/Ir trilayers (Fig. 10) displays the band filling trend in the 4d overlayer and its effect on the hybridization with the Co layer. For the Tc and Ru overlayer the hybridization in the majority spin channel even shifts Co states above the Fermi energy which leads to the relatively strong reduction of the Co magnetic moment. Several of the peaks in the vicinity of the Fermi energy appear at the same energetic position in all three layers, indicating that these are hybrid states between all three atom types. It is also visible how these states shift to lower energies with increasing band filling of the 4d band. The strong hybridization effect is the origin of the drastic change of the spin spiral energy dispersion seen in Fig. 9 for Tc/Co/Ir and Ru/Co/Ir. For Rh and Pd overlayers there is still a significant effect on the Co LDOS, however, the majority spin band of Co

TABLE V. Magnetic moments of the Co based trilayer systems for the ferromagnetic state. All values are given in μ_B.

4d/Co/Ir	m_{4d}	m_{Co}	m_{Ir}
Tc/Co/Ir	−0.12	+1.07	+0.05
Ru/Co/Ir	−0.06	+1.53	+0.16
Rh/Co/Ir	+0.66	+2.05	+0.28
Pd/Co/Ir	+0.35	+2.08	+0.43

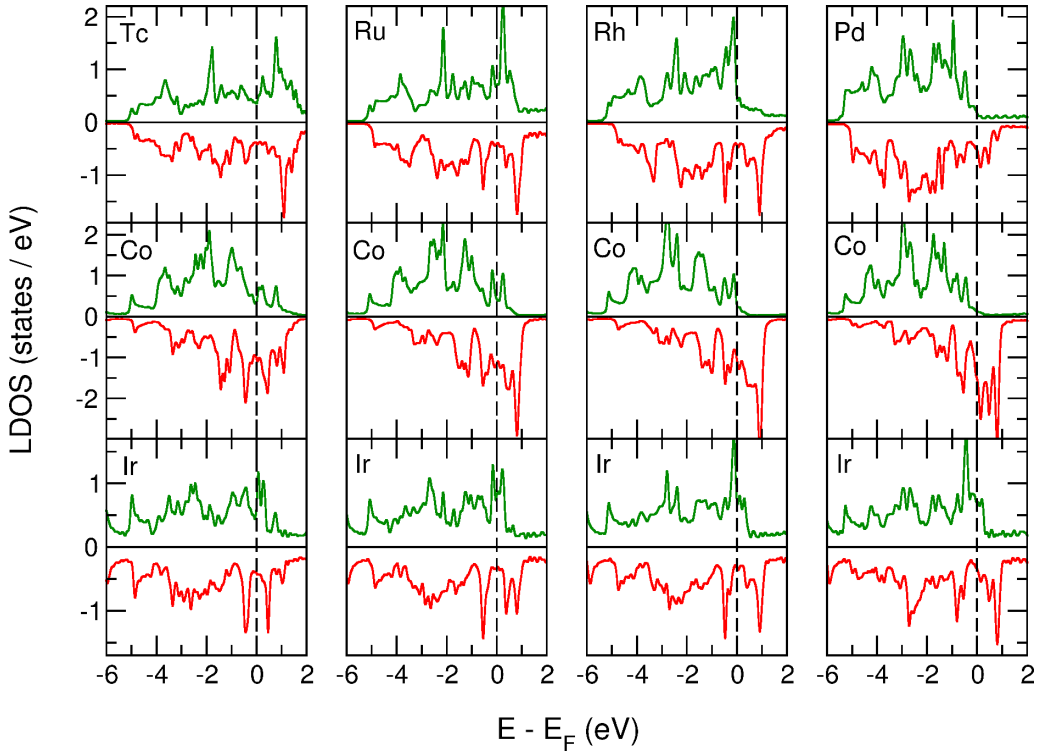

FIG. 10. Local density of states (LDOS) of the fcc-4*d*/Co/Ir trilayers in the ferromagnetic state. The upper panels show the LDOS of the 4*d* overlayer, the middle panels the LDOS of the Co layer, and the lower panels that of the Ir layer. Majority and minority spin channels are represented in green and red color, respectively.

is almost completely filled typical for Co. For Rh/Co/Ir, the majority spin LDOS is still enhanced at the Fermi level and the peaks just below the Fermi energy are hybrid states.

In accordance with the observations from the spin spiral dispersions, Fig. 11(a) presents large values for the exchange constant J_1 of both Rh/Co/Ir and Pd/Co/Ir trilayers as well as the corresponding film systems Rh/Co/Ir(111) and Pd/Co/Ir(111). Starting from about 6.8 meV for Tc/Co/Ir, the NN constant peaks at about 26.4 meV for Rh/Co/Ir. Therefore, the FM exchange coupling between nearest neighbors is much stronger than for the 4*d*/Fe/Ir trilayers. While J_1 can be influenced much less in the Co based trilayers by hybridization with the adjacent 4*d* layer, it still allows a reduction by more than a factor of two for Ru and Tc adlayers.

In contrast to J_1, the next-nearest neighbor constant J_2 is very small with maximum values of up to about -1.5 meV for the Rh/Co/Ir trilayer and only barely noticeable protruding the zero line for the ultrathin film systems. A similar behavior becomes manifest for J_3 with a larger maximum value of about -4.6 meV for Rh/Co/Ir and -2.7 meV for Rh/Co/Ir(111). While the FM pairwise Heisenberg exchange interaction dominates the next-nearest and third nearest neigh-

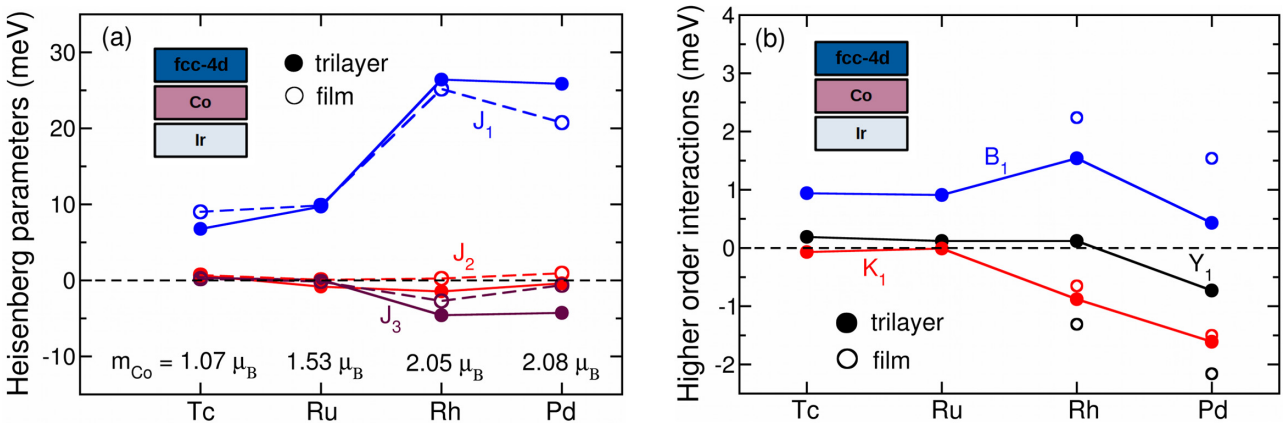

FIG. 11. Trends for both (a) Heisenberg exchange constants up to the third nearest neighbor as extracted from fitting the corresponding spin spiral dispersions, i.e.. without modification by HOI terms, and (b) the HOI parameters Y_1, K_1, and B_1 for fcc-4*d*/Co/Ir trilayers (filled circles and solid lines) and film systems Rh/Co/Ir(111) and Pd/Co/Ir(111) (open circles and dashed lines). The lines connecting the data points serve as a guide to the eye.

TABLE VI. Comparison of the HOI parameters K_1 and B_1 (in meV) for selected trilayer (in fcc-stacking) and film systems calculated from a mixture of FLEUR (*uudd* states, spin spirals) and VASP (3Q states) denoted by the superscript 'mix' and FLEUR only. Note that Y_1 is evaluated from the energy difference between the two *uudd* states which have only been calculated using FLEUR. Therefore, only one value is given. All values are given in meV.

	K_1^{mix}	K_1^{FLEUR}	B_1^{mix}	B_1^{FLEUR}	Y_1
Rh/Fe/Ir	3.33	3.71	2.59	3.35	0.84
Pd/Fe/Ir	3.87	4.30	2.62	3.49	1.29
fcc-Rh/Fe/Ir(111)	2.12	2.48	2.60	3.33	−0.85
hcp-Rh/Fe/Ir(111)	1.94	1.88	4.27	4.14	3.84
Rh/Co/Ir	−1.15	−0.88	0.98	1.54	0.12
Pd/Co/Ir	−1.75	−1.61	0.15	0.43	−0.73
fcc-Rh/Co/Ir(111)	−0.79	−0.58	1.38	1.79	−0.96
fcc-Pd/Co/Ir(111)	−1.53	−1.41	1.36	1.60	−1.39

bor constants mediating mostly an AFM coupling in Co based trilayers, there is a considerable exchange frustration present which leads to the remarkably flat energy dispersion curve close to the FM state especially for Rh/Co/Ir and Rh/Co/Ir(111) [16].

Comparing further the HOI parameters of Co based trilayers and film systems in Fig. 11(b) and Table IV, one notices a similar trend for Y_1, K_1, and B_1 along the trilayer series at first glance. Up to Ru/Co/Ir the three exchange constants nearly stay constant with B_1 showing the largest values of about 1.5 meV for Rh/Co/Ir and K_1 almost vanishing in the case of Tc/Co/Ir and Ru/Co/Ir. Y_1 turns out to be extremely small as well with maximum values of about 0.2 meV occurring for Tc/Co/Ir. This trend considerably reverses for Pd/Co/Ir as Y_1 and K_1 start dropping below zero and taking significant values of $K_1 \approx -1.6$ meV.

The two film systems Rh/Co/Ir(111) and Pd/Co/Ir(111) follow a similar trend as the respective trilayers: K_1 exhibits negative values each with a maximum of about -1.4 meV for Pd/Co/Ir(111), whereas the biquadratic term is positive and on the same order of magnitude for both systems. Comparing further two different stackings of the Rh top layer in the Rh/Co/Ir(111) system, one finds a negative value of K_1 which is nearly twice as large for hcp-Rh as compared to fcc-Rh (see Table IV). The opposite is true for the biquadratic term whose size is approximately five times larger in the fcc case. The negative value of K_1 for Rh/Co/Ir(111) considerably lowers the stability of skyrmions [15] which have been observed in these films at zero magnetic field [16,42].

For comparison, we have studied the symmetric trilayer Rh/Co/Rh which is isoelectronic to Rh/Co/Ir. As seen in Table VII, this approach only causes minor changes for the magnetic exchange constants similar to our finding for Fe based trilayers. With the exception of the three spin term Y_1 that experiences a change of sign, the HOI parameters are on the same order of magnitude as the respective values of Rh/Co/Ir. Our calculations reveal a similar behavior for the spin spiral dispersion of Rh/Co/Rh and Rh/Co/Rh(111) as well [34] (not shown).

TABLE VII. Higher-order exchange constants K_1, B_1, and Y_1 for asymmetric and symmetric Fe and Co based trilayers. The corresponding energy differences of the three multi-Q and the corresponding single-Q states are listed in Table VIII. All values are given in meV.

$4d$/Fe/Ir	K_1	B_1	Y_1
fcc-Tc/Fe/Ir	0.15	−0.11	−1.15
fcc-Ru/Fe/Ir	1.86	1.79	1.22
hcp-Ru/Fe/Ir	2.64	2.15	3.28
fcc-Rh/Fe/Ir	3.33	2.59	0.84
hcp-Rh/Fe/Ir	3.02	5.63	5.32
fcc-Pd/Fe/Ir	3.87	2.62	1.29
hcp-Pd/Fe/Ir	3.31	4.64	3.13
fcc-5d/Fe/Rh			
Re/Fe/Rh	0.76	0.36	−1.10
Os/Fe/Rh	2.28	1.88	1.66
Pt/Fe/Rh	3.50	3.44	1.58
$4d$/Fe/$4d$			
fcc-Tc/Fe/Tc	0.12	0.35	−0.07
fcc-Ru/Fe/Ru	0.81	0.80	1.74
fcc-Rh/Fe/Rh	3.60	1.55	0.90
hcp-Rh/Fe/Rh	3.12	3.81	4.03
fcc-Pd/Fe/Pd	0.94	1.98	1.14
Tc/Co/Ir	−0.07	0.94	0.19
Ru/Co/Ir	−0.01	0.91	0.12
fcc-Rh/Co/Ir	−0.88	1.54	0.12
Pd/Co/Ir	−1.61	0.43	−0.73
fcc-Rh/Co/Rh	−0.66	1.26	−0.27

IV. CONCLUSION

We have presented a systematic first-principles study about the behavior of magnetic exchange interactions in transition metal trilayers with a central Fe or Co layer and compared the results with those obtained for the corresponding ultrathin films on surfaces. We included not only the pairwise Heisenberg exchange interaction but also higher-order contributions arising in fourth order perturbation theory from the Hubbard model. We investigated the effect of the stacking sequence of the trilayers on pairwise exchange constants and on the biquadratic interaction and the three-site and four-site four spin interactions. Trends for these magnetic exchange constants were obtained by replacing the outer layers of the respective trilayer with different elements from the 4d and 5d series. Since there is a strong 3d-4d and 3d-5d hybridization, the band filling has a large impact on both pairwise and higher-order exchange constants. For comparison we analyzed trends for these exchange parameters in symmetric $4d$/Fe/$4d$ systems.

We find that the exchange interactions in Fe and Co layers can be drastically modified due to the hybridization between 3d, 4d, and 5d bands in these sandwich structures. The trend of the interactions with band filling does not depend on using isoelectronic 4d and 5d transition metals. We find a good agreement of the trends between trilayer and film calculations highlighting that the hybridization at the two interfaces is the main origin of the modified exchange interactions.

In Fe based trilayers we find that the magnetic ground state strongly varies upon replacing the adlayers and the ferromagnetic or row-wise antiferromagnetic state as well as spin spiral states can occur. Upon varying the stacking sequence from fcc to hcp, we find that due to higher-order exchange interactions even a superposition state of two spin spirals, the *uudd* ($2Q$) state, can be stabilized in hcp-Rh/Fe/Ir and hcp-Rh/Fe/Rh trilayers. Our calculations of the higher-order exchange constants reveal that this effect, which has been previously observed for Rh/Fe/Ir(111) [13], is dominated by the change of the three-site four spin interaction. For the Rh/Fe/Ir trilayers, the higher-order exchange constants can even be of larger or comparable value than the pairwise exchange interactions. The largest values of the higher-order constants are obtained for the film system Rh/Fe/Rh(111). For Pd/Fe/Ir trilayers and the corresponding film system Pd/Fe/Ir(111) we find large positive values of the four-site four spin interaction constant which will lead to an enhanced stability of magnetic skyrmions.

In Co based trilayers the hybridization with the adjacent transition metal layers can also lead to a large variation of pairwise exchange constants, however, the magnetic ground state remains the ferromagnetic state and the nearest-neighbor exchange dominates. Nevertheless, a strong frustration of exchange interactions can occur. This can lead to magnetic skyrmions being stable in zero magnetic field as in Rh/Co/Ir(111) [16]. The values of the higher-order exchange constants are mostly smaller than in the Fe based trilayers. Importantly, we find that the four-site four spin interaction is negative for all considered Co based trilayers and film systems which will lead to a decreased stability of skyrmions in these systems.

ACKNOWLEDGMENTS

We gratefully acknowledge computing time at the supercomputer of the North-German Supercomputing Alliance (HLRN) and financial support from the Deutsche Forschungsgemeinschaft (DFG, German Research Foundation) via Project No. 418425860 (HE3292/13-1).

APPENDIX A: COMPARISON OF METHODS FOR HOI

In this section we show for selected trilayers and film systems to which extent a mixture of both DFT codes—the all-electron FLAPW method as implemented in FLEUR and the PAW method from VASP which is based on pseudopotentials—can be used to obtain the trends of the HOI parameters. We have chosen two systems from the Fe based and Co based series for which the corresponding film systems have already been studied experimentally [13,16,36–39,41].

We have calculated the energy differences between the two *uudd* states and the corresponding spin spiral states, $\Delta E_{\frac{1}{2}\overline{\Gamma\mathrm{M}}}$ and $\Delta E_{\frac{3}{4}\overline{\Gamma\mathrm{K}}}$ [cf. Eqs. (3) and (4)], using FLEUR while the energy difference between the RW-AFM and the $3Q$ state, Eq. (2), has either been obtained with FLEUR or alternatively with VASP. Using Eqs. (5)–(7) we have obtained the biquadratic term B_1, the three-site four spin term Y_1, and the four-site four spin constant K_1 using only the energy differences from FLEUR (Table VI). We can also use the energy difference $\Delta E_{\overline{\mathrm{M}}}$ obtained via VASP, which is computationally less demanding, and $\Delta E_{\frac{1}{2}\overline{\Gamma\mathrm{M}}}$ and $\Delta E_{\frac{3}{4}\overline{\Gamma\mathrm{K}}}$ from FLEUR. As seen in Table VI the biquadratic and four-site four spin terms change upon using this mixed approach. Note that only one value of Y_1 is given in Table VI since it is obtained according to Eq. (6) from the difference of $\Delta E_{\frac{1}{2}\overline{\Gamma\mathrm{M}}}$ and $\Delta E_{\frac{3}{4}\overline{\Gamma\mathrm{K}}}$.

For the Fe based trilayers, one sees that the values for the four-site four spin term K_1 are by about 10% larger for the all-electron FLAPW method (K_1^{FLEUR}) than for the mixture of both DFT codes (K_1^{mix}). However, the sign of K_1 is the same in both methods for the Rh/Fe/Ir and Pd/Fe/Ir trilayer. The same holds for the biquadratic term B_1 albeit the values calculated using FLEUR are larger by about 20% than for the mixed method. A similar trend is obtained for the film systems Rh/Fe/Ir(111). Therefore, we conclude that the mixed

TABLE VIII. Total energy differences between multi-Q and their corresponding single-Q states defined according to Eqs. (2)–(4) used to calculate the HOI terms within NN approximation according to Eqs. (5)–(7) in Sec. III of the main text (Table VII and IV). All values are given in meV/Fe atom.

$4d$/Fe/Ir	$\Delta E_{\frac{1}{2}\overline{\Gamma\mathrm{M}}}$	$\Delta E_{\frac{3}{4}\overline{\Gamma\mathrm{K}}}$	$\Delta E_{\overline{\mathrm{M}}}$
fcc-Tc/Fe/Ir	6.21	−2.96	7.16
fcc-Ru/Fe/Ir	2.84	12.60	22.83
hcp-Ru/Fe/Ir	−0.58	25.68	22.18
fcc-Rh/Fe/Ir	12.95	19.66	44.88
hcp-Rh/Fe/Ir	−19.67	22.85	33.86
fcc-Pd/Fe/Ir	15.29	25.58	48.36
hcp-Pd/Fe/Ir	−4.59	20.45	43.37
fcc-Rh/Fe/Ir(111)	9.92	3.11	48.72
hcp-Rh/Fe/Ir(111)	−16.90	13.82	21.61
fcc-Pd/Fe/Ir(111)	0.23	17.41	36.36
hcp-Pd/Fe/Ir(111)	4.46	21.62	22.66
fcc-$5d$/Fe/Rh			
Re/Fe/Rh	9.05	0.27	15.90
Os/Fe/Rh	4.11	17.37	25.50
Pt/Fe/Rh	7.89	20.51	47.22
$4d$/Fe/$4d$			
fcc-Tc/Fe/Tc	−0.19	−0.75	3.47
fcc-Ru/Fe/Ru	−3.70	10.19	3.62
fcc-Rh/Fe/Rh	18.96	26.19	41.87
hcp-Rh/Fe/Rh	−6.42	25.82	32.17
fcc-Pd/Fe/Pd	−4.95	4.14	14.53
fcc-Rh/Fe/Rh(111)	9.87	18.71	42.96
hcp-Rh/Fe/Rh(111)	−24.17	16.77	30.49
$4d$/Co/Ir			
fcc-Tc/Co/Ir	−5.07	−3.55	3.31
fcc-Ru/Co/Ir	4.20	−3.28	4.07
fcc-Rh/Co/Ir	−13.65	−12.68	−1.82
fcc-Pd/Co/Ir	−11.71	−17.53	−10.99
fcc-Rh/Co/Rh	−9.27	−11.42	1.08
fcc-Rh/Co/Ir(111)	−8.01	−15.65	8.43
hcp-Rh/Co/Ir(111)	−3.29	−15.65	−0.71
fcc-Pd/Co/Ir(111)	−12.08	−23.22	0.95

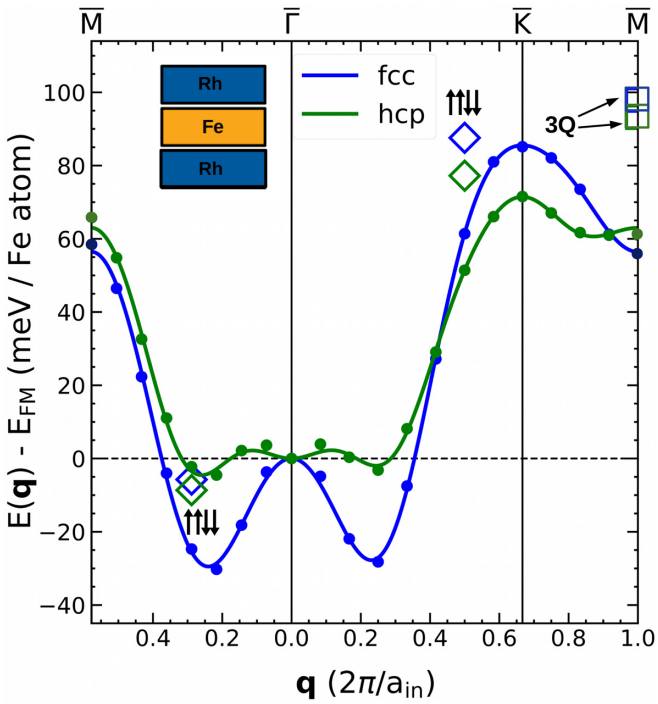

FIG. 12. Energy dispersion of flat spin spirals for Rh/Fe/Rh trilayers. Total energies calculated by DFT are marked by filled circles, whereas the solid lines represent fits to the Heisenberg model. Both energies of the *uudd* (↑↑↓↓) states as well as the 3Q state are plotted as empty diamonds and squares at the q values of the corresponding single-Q states, respectively.

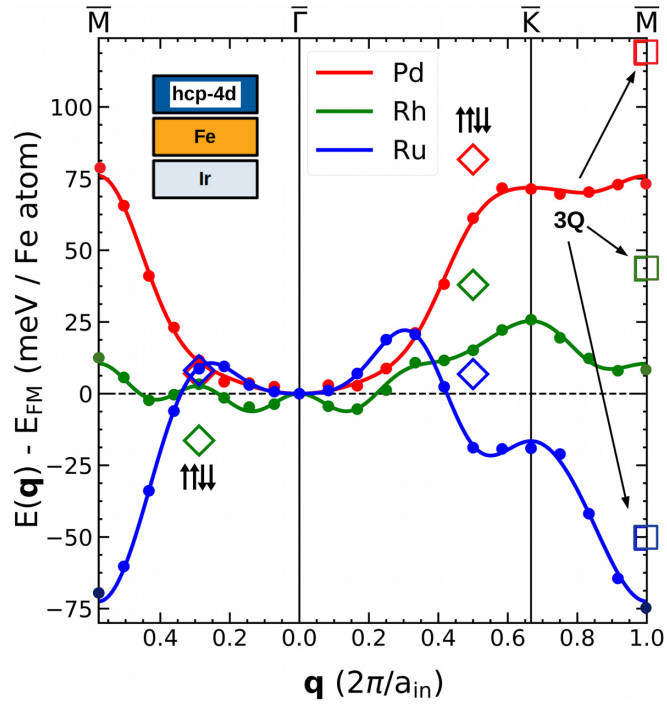

FIG. 13. Energy dispersion of flat spin spirals for hcp-4d/Fe/Ir trilayers. Total energies calculated by DFT are marked by filled circles, whereas the solid lines represent fits to the Heisenberg model. Both energies of the *uudd* (↑↑↓↓) states as well as the 3Q state are plotted as empty diamonds and squares at the q values of the corresponding single-Q states, respectively.

approach provides reliable values of the HOI parameters even if the less demanding approach is used in which the non-collinear 3Q state is calculated via VASP.

For the two Co based trilayers, the sign of K_1 and B_1 is again the same in both approaches. However, the relative differences are larger and there is no clear trend. This becomes not only noticeable for Rh/Co/Ir where the deviation of B_1 from FLEUR amounts to 36%, but also for B_1 in the Pd/Co/Ir trilayer showing a value which is by 65% larger for FLEUR than for the mixed method (Table VI). Interestingly, the deviations are smaller for the Co based ultrathin film systems as compared to the trilayers (see Table VI). While the maximum deviation amounts to 36% for K_1 in case of fcc-Rh/Co/Ir(111), the differences become very small for both K_1 as well as B_1 in fcc-Pd/Co/Ir(111). Hence we conclude that in principle the combined approach of FLEUR and VASP yields acceptable results for calculating HOI parameters both in Fe based as well as Co based ultrathin film systems. However, it is critical to use the same number of Ir substrate layers for the computation of energy dispersions of spin spirals and multi-Q states.

Summarizing the results of our calculations, we conclude that a combined approach of two different DFT codes—FLEUR and VASP—represents an acceptable and computationally less demanding way of calculating trends of HOI parameters in Fe based trilayers and film systems. Therefore, we used this approach for the other Fe based trilayers as described in Sec. II B. For the Co based trilayers the deviations were larger and therefore we used the FLEUR code to calculate all required total energy differences. While the deviations were reasonable for the Co based film system we still used only FLEUR in order to be consistent with the trilayer calculations.

APPENDIX B: ENERGY DIFFERENCES MULTI-Q VS. SINGLE-Q STATES FOR EVALUATION OF HOI TERMS

In the main part of the paper we discussed the trends of HOI constants in Fe and Co based trilayers mainly by analyzing the data on figures. For the sake of completeness, we list the energy differences of multi-Q vs. single-Q states for all studied systems within the paper: trilayers as well as ultrathin film systems (see Table VIII). The respective HOI terms given in the main text were then calculated according to Eqs. (5)–(7).

APPENDIX C: ENERGY DISPERSION OF hcp-Rh/Fe/Rh AND hcp-4d/Fe/Ir TRILAYERS

Here we show the energy dispersion of hcp-Rh/Fe/Rh and hcp-4d/Fe/Ir trilayers for the comparison of fcc vs. hcp stacking [cf. Figs. 5(a), 12 and 13]. Note, that the *uudd* state is the energetically lowest state for hcp-Rh/Fe/Rh and hcp-Rh/Fe/Ir while for fcc-Rh/Fe/Rh and fcc-Rh/Fe/Ir a spin spiral state is the magnetic ground state.

[1] M. Takahashi, Half-filled Hubbard model at low temperature, J. Phys. C **10**, 1289 (1977).

[2] A. H. MacDonald, S. M. Girvin, and D. Yoshioka, $\frac{t}{U}$ expansion for the Hubbard model, Phys. Rev. B **37**, 9753 (1988).

[3] M. Hoffmann and S. Blügel, Systematic derivation of realistic spin models for beyond-Heisenberg solids, Phys. Rev. B **101**, 024418 (2020).

[4] M. Albrecht, M. Maret, J. Köhler, B. Gilles, R. Poinsot, J. L. Hazemann, J. M. Tonnerre, C. Teodorescu, and E. Bucher, Ferromagnetic hcp Chromium in Cr/Ru(0001) Superlattices, Phys. Rev. Lett. **85**, 5344 (2000).

[5] D. Repetto, T. Y. Lee, S. Rusponi, J. Honolka, K. Kuhnke, V. Sessi, U. Starke, H. Brune, P. Gambardella, C. Carbone, A. Enders, and K. Kern, Structure and magnetism of atomically thin Fe layers on flat and vicinal Pt surfaces, Phys. Rev. B **74**, 054408 (2006).

[6] P. Kurz, G. Bihlmayer, K. Hirai, and S. Blügel, Three-Dimensional Spin Structure on a Two-Dimensional Lattice: Mn/Cu(111), Phys. Rev. Lett. **86**, 1106 (2001).

[7] J. Spethmann, S. Meyer, K. von Bergmann, R. Wiesendanger, S. Heinze, and A. Kubetzka, Discovery of Magnetic Single- and Triple-Q States in Mn/Re(0001), Phys. Rev. Lett. **124**, 227203 (2020).

[8] Y. Yoshida, S. Schröder, P. Ferriani, D. Serrate, A. Kubetzka, K. von Bergmann, S. Heinze, and R. Wiesendanger, Conical Spin-Spiral State in an Ultrathin Film Driven by Higher-Order Spin Interactions, Phys. Rev. Lett. **108**, 087205 (2012).

[9] S. Heinze, K. von Bergmann, M. Menzel, J. Brede, A. Kubetzka, R. Wiesendanger, G. Bihlmayer, and S. Blügel, Spontaneous atomic-scale magnetic skyrmion lattice in two dimensions, Nat. Phys. **7**, 713 (2011).

[10] B. Hardrat, A. Al-Zubi, P. Ferriani, S. Blügel, G. Bihlmayer, and S. Heinze, Complex magnetism of iron monolayers on hexagonal transition metal surfaces from first principles, Phys. Rev. B **79**, 094411 (2009).

[11] A. Al-Zubi, G. Bihlmayer, and S. Blügel, Modelling magnetism of hexagonal Fe monolayers on 4d substrates, Phys. Status Solidi B **248**, 2242 (2011).

[12] A. Krönlein, M. Schmitt, M. Hoffmann, J. Kemmer, N. Seubert, M. Vogt, J. Küspert, M. Böhme, B. Alonazi, J. Kügel, H. A. Albrithen, M. Bode, G. Bihlmayer, and S. Blügel, Magnetic Ground State Stabilized by Three-Site Interactions: Fe/Rh(111), Phys. Rev. Lett. **120**, 207202 (2018).

[13] N. Romming, H. Pralow, A. Kubetzka, M. Hoffmann, S. von Malottki, S. Meyer, B. Dupé, R. Wiesendanger, K. von Bergmann, and S. Heinze, Competition of Dzyaloshinskii-Moriya and Higher-Order Exchange Interactions in Rh/Fe Atomic Bilayers on Ir(111), Phys. Rev. Lett. **120**, 207201 (2018).

[14] W. Li, S. Paul, K. von Bergmann, S. Heinze, and R. Wiesendanger, Stacking-Dependent Spin Interactions in Pd/Fe Bilayers on Re(0001), Phys. Rev. Lett. **125**, 227205 (2020).

[15] S. Paul, S. Haldar, S. Malottki, and S. Heinze, Role of higher-order exchange interactions for skyrmion stability, Nat. Commun. **11**, 4756 (2020).

[16] S. Meyer, M. Perini, S. Malottki, A. Kubetzka, R. Wiesendanger, K. von Bergmann, and S. Heinze, Isolated zero field sub-10 nm skyrmions in ultrathin Co films, Nat. Commun. **10**, 3823 (2019).

[17] See https://www.flapw.de.

[18] See https://www.vasp.at.

[19] J. Hubbard, Electron Correlations in Narrow Energy Bands, Proc. R. Soc. London Ser., A **276**, 238 (1963).

[20] S. Brinker, M. dos Santos Dias, and S. Lounis, The chiral biquadratic pair interaction, New J. Phys. **21**, 083015 (2019).

[21] S. Brinker, M. dos Santos Dias, and S. Lounis, Prospecting chiral multisite interactions in prototypical magnetic systems, Phys. Rev. Research **2**, 033240 (2020).

[22] S. Mankovsky, S. Polesya, and H. Ebert, Extension of the standard Heisenberg Hamiltonian to multispin exchange interactions, Phys. Rev. B **101**, 174401 (2020).

[23] A. Lászlóffy, L. Rózsa, K. Palotás, L. Udvardi, and L. Szunyogh, Magnetic structure of monatomic Fe chains on Re(0001): Emergence of chiral multispin interactions, Phys. Rev. B **99**, 184430 (2019).

[24] P. Kurz, Non-collinear magnetism at surfaces and in ultrathin films, Ph.D. thesis, Rheinisch-Westfälische Technische Hochschule Aachen, 2000.

[25] D. R. Hamann, Semiconductor Charge Densities with Hard-Core and Soft-Core Pseudopotentials, Phys. Rev. Lett. **42**, 662 (1979).

[26] E. Wimmer, H. Krakauer, M. Weinert, and A. J. Freeman, Full-potential self-consistent linearized-augmented-plane-wave method for calculating the electronic structure of molecules and surfaces: O_2 molecule, Phys. Rev. B **24**, 864 (1981).

[27] P. E. Blöchl, Projector augmented-wave method, Phys. Rev. B **50**, 17953 (1994).

[28] G. Kresse and D. Joubert, From ultrasoft pseudopotentials to the projector augmented-wave method, Phys. Rev. B **59**, 1758 (1999).

[29] G. Kresse and J. Furthmüller, Efficient iterative schemes for ab initio total-energy calculations using a plane-wave basis set, Phys. Rev. B **54**, 11169 (1996).

[30] S. H. Vosko, L. Wilk, and M. Nusair, Accurate spin-dependent electron liquid correlation energies for local spin density calculations: a critical analysis, Can. J. Phys. **58**, 1200 (1980).

[31] P. Ferriani, K. von Bergmann, E. Y. Vedmedenko, S. Heinze, M. Bode, M. Heide, G. Bihlmayer, S. Blügel, and R. Wiesendanger, Atomic-Scale Spin Spiral with a Unique Rotational Sense: Mn Monolayer on W(001), Phys. Rev. Lett. **101**, 027201 (2008).

[32] B. Dupé, M. Hoffmann, C. Paillard, and S. Heinze, Tailoring magnetic skyrmions in ultra-thin transition metal films, Nat. Commun. **5**, 4030 (2014).

[33] S. Meyer, B. Dupé, P. Ferriani, and S. Heinze, Dzyaloshinskii-Moriya interaction at an antiferromagnetic interface: First-principles study of Fe/Ir bilayers on Rh(001), Phys. Rev. B **96**, 094408 (2017).

[34] S. Meyer, Complex spin structures in frustrated ultrathin films, Ph.D. thesis, Christian-Albrechts-Universität zu Kiel, 2020.

[35] M. M. Sigalas and D. A. Papaconstantopoulos, Calculations of the total energy, electron-phonon interaction, and Stoner parameter for metals, Phys. Rev. B **50**, 7255 (1994).

[36] N. Romming, C. Hanneken, M. Menzel, J. E. Bickel, B. Wolter, K. von Bergmann, A. Kubetzka, and R. Wiesendanger, Writing and deleting single magnetic skyrmions, Science **341**, 636 (2013).

[37] N. Romming, A. Kubetzka, C. Hanneken, K. von Bergmann, and R. Wiesendanger, Field-Dependent Size and Shape of Single Magnetic Skyrmions, Phys. Rev. Lett. **114**, 177203 (2015).

[38] C. Hanneken, F. Otte, A. Kubetzka, B. Dupé, N. Romming, K. von Bergmann, R. Wiesendanger, and S. Heinze, Electrical detection of magnetic skyrmions by non-collinear magnetoresistance, Nat. Nanotechnol. **10**, 1039 (2015).

[39] A. O. Leonov, T. L. Monchesky, N. Romming, A. Kubetzka, A. N. Bogdanov, and R. Wiesendanger, The properties of isolated chiral skyrmions in thin magnetic films, New J. Phys. **18**, 065003 (2016).

[40] Note that we could not converge calculations for the hcp-Tc/Fe/Ir trilayer.

[41] L. V. Dzemiantsova, M. Hortamani, C. Hanneken, A. Kubetzka, K. von Bergmann, and R. Wiesendanger, Magnetic coupling of single Co adatoms to a Co underlayer through a Pd spacer of variable thickness, Phys. Rev. B **86**, 094427 (2012).

[42] M. Perini, S. Meyer, A. Kubetzka, R. Wiesendanger, S. Heinze, and K. von Bergmann, Electrical Detection of Domain Walls and Skyrmions in Co Films Using Noncollinear Magnetoresistance, Phys. Rev. Lett. **123**, 237205 (2019).